









## Article

# A Previously Unknown Building Structure in Ancient Olympia (Western Peloponnese, Greece) Revealed by Geoarchaeological Investigations and Its Interpretation as a Possible Harbor

Lena Slabon <sup>1,\*</sup>, Sarah Bäumler <sup>2</sup>, Elena Appel <sup>1</sup>, Sabine Fiedler <sup>1</sup>, Peter Fischer <sup>1</sup>, Lea Obrocki <sup>1</sup>, Georg Pantelidis <sup>3</sup>, Sascha Scherer <sup>1</sup>, Benedict Thein <sup>1</sup>, Timo Willershäuser <sup>1</sup>, Birgitta Eder <sup>4</sup>, Hans-Joachim Gehrke <sup>5</sup>, Franziska Lang <sup>3</sup>, Erofilii-Iris Kolia <sup>6</sup>, Oliver Pilz <sup>7</sup>, Dennis Wilken <sup>2</sup> and Andreas Vött <sup>1,\*</sup>

<sup>1</sup> Institute of Geography, Johannes Gutenberg-Universität Mainz, 55122 Mainz, Germany; eappel02@uni-mainz.de (E.A.); fiedlers@uni-mainz.de (S.F.); fischep@uni-mainz.de (P.F.); lobrocki@uni-mainz.de (L.O.); s.scherer@geo.uni-mainz.de (S.S.); b.thein@geo.uni-mainz.de (B.T.); timo.willershaeuser@uni-mainz.de (T.W.)

<sup>2</sup> Institute of Geosciences, Kiel University, 24118 Kiel, Germany; sarah.baemler@ifg.uni-kiel.de (S.B.); dennis.wilken@ifg.uni-kiel.de (D.W.)

<sup>3</sup> Department of Classical Archaeology, Technische Universität Darmstadt, 64289 Darmstadt, Germany; gpantelidis@klarch.tu-darmstadt.de (G.P.); flang@klarch.tu-darmstadt.de (F.L.)

<sup>4</sup> Austrian Academy of Sciences, Austrian Archaeological Institute, 10683 Athens, Greece; birgitta.eder@oeaw.ac.at

<sup>5</sup> Seminar of Ancient History, Universität Freiburg, 79098 Freiburg, Germany; hj-g-gehrke@t-online.de

<sup>6</sup> Ephorate of Prehistoric and Classical Antiquities of Ilia, 27065 Ancient Olympia, Greece; ekollia@culture.gr

<sup>7</sup> Athens Department, German Archaeological Institute, 10678 Athens, Greece; oliver.pilz@dainst.de

\* Correspondence: lslabon@uni-mainz.de (L.S.); voett@uni-mainz.de (A.V.)

**Abstract:** The ancient site of Olympia is located on the northern fringe of the Basin of Makrisia at the confluence of the Kladeos and Alpheios rivers (western Peloponnese, Greece) and was used as a venue for the Panhellenic Games from Archaic times until the 4th century AD. Geophysical prospection (frequency domain electromagnetic induction and electrical resistivity tomography) was carried out as a basis for detailed geoarchaeological investigations. In doing so, we identified a previously unknown building structure adjacent to the Altis, the inner part of the sanctuary at Olympia. Situated south of the Southwest Thermae, this structure measures at least 100 m (WSW-ENE) by 80 m (NNW-SSE). Its external orientation is in line with the orientation of the Southwest Thermae and the Leonidaion. We retrieved sediment cores from 17 different locations in combination with high-resolution direct push sensing from inside the newly found structure. All cores revealed distinct units of organic-rich limnic sediments dominated by clay and fine silt. Geochemical and micropaleontological analyses of selected sediment samples indicate highly eutrophic conditions, as evidenced by elevated phosphorous concentrations and the dominance of the ostracod species *Cyprideis torosa*, which is able to live under low-oxygen conditions. Moreover, molecular biomarker analyses show a significant input of lipid fecal markers, implying strong anthropogenic pollution. Further, the limnic sediments include numerous charcoal remains and abundant diagnostic artifacts such as ceramic fragments and building material. Radiocarbon dating documents that these limnic conditions persisted within the building structure from at least the 5th century BC to the 6th century AD. The identified building structure lies in the immediate proximity to the Lake of Olympia, which was recently found to have existed from the mid-Holocene to the Medieval period. Its characteristic filling with fine-grained sediments and multiple indications for a strongly polluted and heavily used standing water environment let us hypothesize that it was



Academic Editor: Mario Bentivenga

Received: 22 November 2024

Revised: 1 January 2025

Accepted: 7 January 2025

Published: 22 January 2025

**Citation:** Slabon, L.; Bäumler, S.; Appel, E.; Fiedler, S.; Fischer, P.; Obrocki, L.; Pantelidis, G.; Scherer, S.; Thein, B.; Willershäuser, T.; et al. A Previously Unknown Building Structure in Ancient Olympia (Western Peloponnese, Greece) Revealed by Geoarchaeological Investigations and Its Interpretation as a Possible Harbor. *Heritage* **2025**, *8*, 38. <https://doi.org/10.3390/heritage8020038>

**Copyright:** © 2025 by the authors. Licensee MDPI, Basel, Switzerland. This article is an open access article distributed under the terms and conditions of the Creative Commons Attribution (CC BY) license (<https://creativecommons.org/licenses/by/4.0/>).

possibly used as a harbor installation. A harbor at ancient Olympia could have been used to reach the sanctuary by boat and to transport goods of all kinds.

**Keywords:** ancient Olympia; geoarchaeology; sediment coring; direct push sensing; geochemical analyses; micropalaeontology; biomarker analyses; western Peloponnese; Greece

---

## 1. Introduction

The ancient site of Olympia is known as a venue for the Panhellenic Games between Archaic times and the 4th century AD as well as for the sanctuary dedicated to Zeus [1,2]. The site is located in the Basin of Makrisia, in the western part of the Peloponnese, close to the Gulf of Kyparissia. During the Panhellenic Games, the cult site hosted numerous visitors [1,3]. However, the site lost its significance with the prohibition of the pagan cult in the late 4th century and was later buried under a thick layer of debris and sediment. Ancient Olympia remained untouched until its rediscovery by the English theologian and traveler Richard Chandler in 1766, who noticed remains of the Temple of Zeus emerging from the sedimentary cover [4–6]. The first excavations were carried out by a French mission in 1829 [3,7]. Systematic excavations of the Altis, the inner part of the cult site, started in 1875 by the German Archaeological Institute [6]. The ancient site is one of the best-investigated cult sites in Greece, even though it has not yet been completely excavated [1]. However, the question of how the original landscape looked alike and how it has changed through natural and anthropogenic processes is still unsolved. Recently, it has been found that a large lake environment existed in the immediate vicinity of ancient Olympia between the mid-Holocene and Medieval times [8,9]. This so-called Lake of Olympia covered large parts of the basins of Makrisia and adjacent Ladiko. The existence of a lake next to the ancient site has archaeological and historical implications for the spatial network of Olympia; also, it would suggest harbor installations at the lake shore [8]. However, neither previous investigations nor historical sources revealed any indications of such infrastructure. During our field campaigns in 2021 and 2023, we investigated an area directly south of the ancient site at the presumed shore of the Lake of Olympia using a multi-proxy approach. Based on geophysical prospection and the detailed analysis of numerous sediment cores, we were able to detect a previously unknown building structure covered by up to 4–6 m of sediment. Our main objectives were (1) to analyze the size, orientation, and form of the building structure, (2) to examine its filling and sedimentary cover to reconstruct the former setting and subsequent landscape dynamics, and (3) to interpret further (geo-)archaeological features regarding a former use of the building structure. In doing so, we aim to consider the natural, socio-political, economic, and cultural nexus of Olympia and its surroundings. In this paper, the main focus is laid on the geoarchaeological interpretation of multi-proxy sediment analyses. The final verification of the discovered building structure is only possible with archaeological excavation, which will hopefully be initiated by this study.

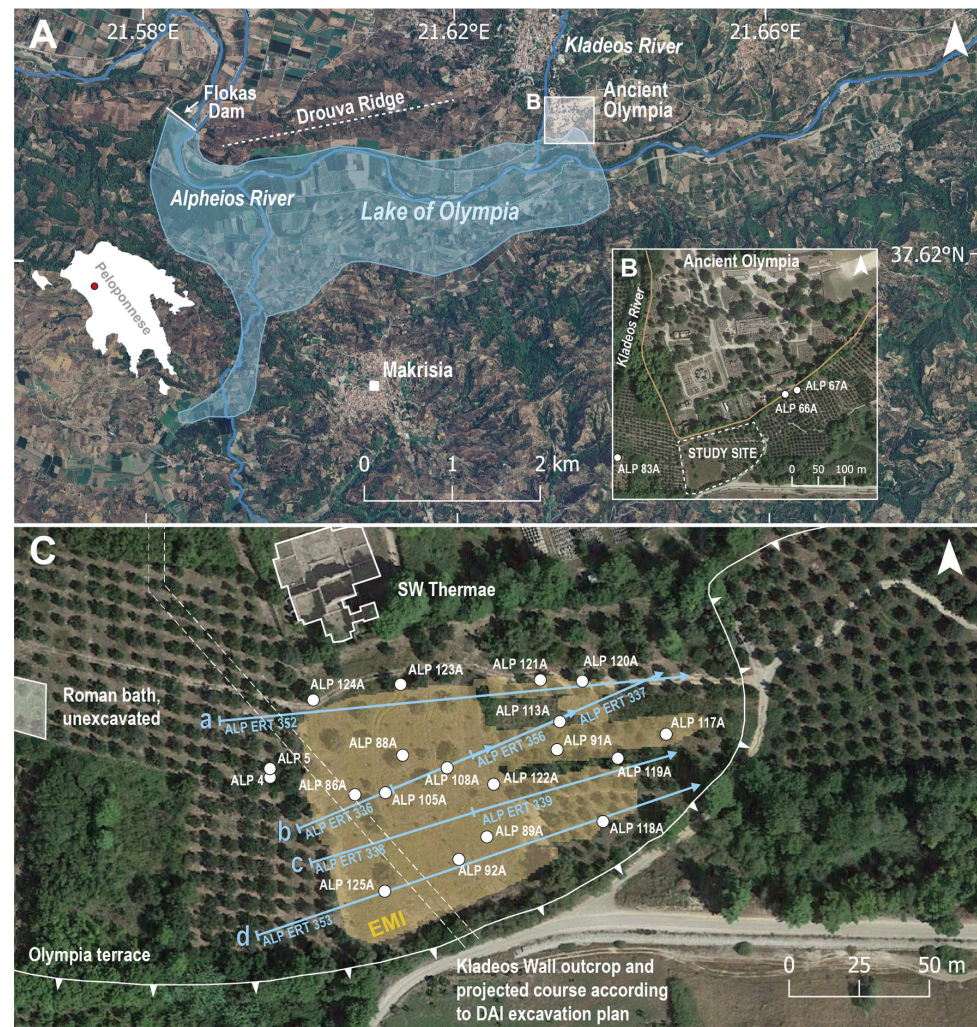
## 2. Regional Setting and Historical Background

### 2.1. Regional Setting

Ancient Olympia is located at the confluence of the Alpheios River and the Kladeos River at the northern fringe of the Basin of Makrisia (Figure 1). The Basin of Makrisia covers a length of 5.5 km and a width of 1.8 km.

The Alpheios River originates in the highlands of Arcadia, flows through the Basin of Makrisia and drains into the Gulf of Kyparissia. At the natural constriction of the Basin of

Makrisia near Flokas, the river temporarily leaves its predominant E-W course and breaks through the Drouva Ridge, where it is nowadays dammed by the Flokas hydro-power dam.



**Figure 1.** Topographic overview of the Basin of Makrisia and the area around the ancient cult site of Olympia (western Peloponnese). (A) The Basin of Makrisia showing the extent of the Lake of Olympia as reconstructed based on sedimentary evidence [9]. (B) Detailed view of ancient Olympia with the location of the study area of this paper to the immediate south of the excavated and fenced archaeological site. (C) Detailed view of the study area south of the Southwest Thermae. White dots mark coring sites; blue lines depict transects along which ERT measurements were carried out; area shaded in yellow marks the area of the EMI survey; white line with triangles marks the edge of the Olympia Terrace; dashed lines delineate the suggested course of the unexcavated Kladeos Wall towards the northwest from its outcrop at the front of the Olympia Terrace.

The Kladeos River originates at Mount Foloe north of Olympia and is a tributary of the Alpheios River [4,10]. The Basin of Makrisia is characterized by Holocene Terrace sediments and alluvial sediments, including the Olympia Terrace [4,11,12]. The latter can be found upstream the Flokas Dam up to the ancient site of Olympia and in parts of the lower and middle Kladeos Valley [4,12]. The northern fringe of the basin, the Drouva Ridge, is composed of Pleistocene conglomerates of the Lalas stage, whereas the southern fringe consists of sand and silt classified as Pliocene Vounargon stage. However, the bedrock in the Kladeos Valley mainly consists of Pliocene marl [11].

The region around Olympia is characterized by a complex system of fault zones [13], which have caused crust uplift of 13–30 m over the last 6400 years [12,14]. Recent geomorphological studies suggest that this uplift occurred in late Medieval times and initiated

major changes in the fluvial landscape by triggering landslides, the formation of landslide-dammed lakes and subsequent lake outbursts in the vicinity of ancient Olympia [9]. Additionally, the wider region is exposed to various natural hazards, such as earthquakes and tsunamis, due to its proximity to the Hellenic Trench [4,15].

## 2.2. Historical Background

The ancient site has a rich history, with the earliest settlement activities dating back to around 3000 BC [16,17]. The cult of Zeus started in the 11th century BC [3,16,18]. By the 8th century BC, the sanctuary had already gained significance beyond its region [3,16]. The beginning of the Panhellenic Games may date back to the early 7th century BC [16,19]. Around 146 BC, the Peloponnese, including Olympia, came under Roman control with the conquest of Corinth [20]. The Roman influence is evident in numerous construction measures in the cult site, although initially, there were no direct effects on the Panhellenic Games [21]. In 393 AD, however, the last Panhellenic Games took place because pagan worship was banned by the law of the Roman emperor Theodosius [1,21]. Still, it is presumed that competitions continued until the 5th century AD [16,20,22]. Subsequently, the site was converted into a vestigial settlement, primarily inhabited by wine growers and craftsmen, with the last signs of settlement activity in the second half of the 7th century AD [22,23].

Based on numerous wells and the reconstructed size of the stadium, it is estimated that 40,000–50,000 visitors were present during the Panhellenic Games [1,3]. Thus, providing adequate infrastructure posed a logistical challenge [3]. According to written accounts and archaeological findings, food was supplied through many vending stalls. The preparation of meat on a large scale is evidenced by numerous iron skewers [1]. Bone remains from sacrificial offerings at the Artemis temple were examined and identified as 78.1% sheep and goats, 17.5% cattle, 3.6% pigs, and 0.3% dogs [24]. Similar findings were obtained by investigations at the Pelopion, where the majority of animal remains consisted of sheep, goats, and cattle, with smaller proportions of pigs and deer [18,21]. For the supply of the site with drinking water, the Alpheios River and the Kladeos River were not suitable, but their water could only be used for washing and watering animals. Instead, drinking water was supplied through temporary wells and, since Classical times, via an aqueduct from the Kladeos Valley [3]. Visitors were accommodated in guesthouses, such as the Leonidaion, in simple tents or shelters [1]. It is further assumed that the festival grounds extended into the Alpheios Valley and were used as a campsite [1].

## 3. Materials and Methods

The study area is located immediately south of the enclosed part of the cult site and was investigated using geophysical, geomorphological, sedimentological, micropalaeontological, and pedological methods to analyze the building structure, its filling and overlying sediments. Field data were collected during two field campaigns in 2021 and 2023. Topographic measurements were made using the Differential Global Positioning System (DGPS) (Topcon HIPER V, Tokyo, Japan with the Getac handheld PS336, Baoshan Township, Taiwan).

### 3.1. Geophysical Prospection and Direct Push Sensing

Over the last decades, electrical resistivity tomography (ERT) developed into a standard method in geoarchaeological research to map the stratigraphic composition of the shallow subsurface (e.g., [14,25–29]) and to detect buried archaeological structures [30,31]. In this study, we carried out ERT measurements primarily with the aim of locating the most suitable coring points. In addition to the geoarchaeological-sedimentological focus presented in this paper, detailed geophysical investigations were carried out and are summarized in [32]. ERT transects were conducted using a Syscal R1 Plus Switch 48 multi-

electrode system (Iris instruments, Orléans, France) and a Wenner–Schlumberger electrode array. The electrode spacing ranges from 1.5 to 3.5 m. ERT data were processed using the RES2DINV software ([https://id.seequent.com/oauth2/authz/?client\\_id=MySeequent-efulEAmErmapeSarInKisMiA&response\\_type=code&scope=openid%20email%20profile%20address&redirect\\_uri=https://my.seequent.com/auth/token&state=eG5hbm8yOGRqaFN4bERJSFVLeGJLcGZhc2NodjNvZ2Rad1BRaVFRNWIPaHFqSTVWWHFCNUNVREg3MFAI MmYIMmZBVHU=](https://id.seequent.com/oauth2/authz/?client_id=MySeequent-efulEAmErmapeSarInKisMiA&response_type=code&scope=openid%20email%20profile%20address&redirect_uri=https://my.seequent.com/auth/token&state=eG5hbm8yOGRqaFN4bERJSFVLeGJLcGZhc2NodjNvZ2Rad1BRaVFRNWIPaHFqSTVWWHFCNUNVREg3MFAI MmYIMmZBVHU=) accessed on 21 November 2024) by applying least-squares inversion using a quasi-Newton method [33]. We used an initial damping factor of 0.10 and a minimum damping factor of 0.03. The root mean square (RMS) convergence limit was set to 5%. Electromagnetic induction (EMI) is a non-invasive method that can be used to determine the distribution of electrical resistance/conductivity of the subsurface and to detect archaeological structures [34]. The method allows for a quick area-wide measurement and was used in this study to obtain a first comprehensive overview of the site. In frequency domain EMI (FDEMI), an electromagnetic field of fixed frequency is created. This primary field induces eddy currents in the subsurface, which generate a secondary electromagnetic field. Depending on the electrical conductivity and magnetic susceptibility of the subsoil, the secondary field undergoes a change of amplitude and phase, which can be measured [35]). We used a CMD Explorer EMI device from GF Instruments (Brno-Medlány, Czech Republic). The device consists of four coils, one transmitting coil, and three receiver coils with a spacing of 1.48 m, 2.82 m, and 4.49 m. The maximum penetration depth is about 6 m (e.g., [36]). The coils were oriented horizontally coplanar (HCP). Acquisition was carried out in continuous mode, meaning the device was moved along profiles on the ground level while measuring GPS position and data. The data sampling rate was 0.1 s, and the position was recorded with the real-time kinematic (RTK) differential global navigation satellite system (DGNSS) (Stonex S9i, Stonex Srl, Paderno, Italy). The data were conducted at a sampling rate of 10 Hz and a signal frequency of 10 kHz, with profile spacing set at 2.5 m. Data processing included coordinate smoothing using a running mean of 11 data points and coordinate correction to align with the center of each coil pair. The processed data were gridded and subjected to linear 2D interpolation on a rectangular grid with a resolution of 0.8 m. Additionally, a 2D median filter with a window size of  $3 \times 3$  bins was applied. Drift correction was not performed, as observed drift effects were less than 5%. Data were binned on a grid of 0.8 m cell size, creating maps for each coil distance (cond1: 1.48 m, cond2: 2.82 m, and cond3: 4.49 m). For details of the setup, see [36].

Direct push (DP) measurements were carried out using a Geoprobe 540MT (Geoprobe Systems, Salina, KS, USA) mounted on an automotive Nordmeyer drill rig (RS 0/2.3 Nordmeyer SMAG, Braunschweig, Germany). To measure electrical conductivity (EC), hydraulic water pressure, and inline pressure, we utilized a Geoprobe K6050 Hydraulic Profiling Tool (HPT) and a Geoprobe OP 6560 Optical Image Profiler (OIP) probe. The Geoprobe K6050 HPT probe measures electrical conductivity using a Wenner electrode array, whereas Geoprobe OP 6560 OIP uses a dipole array. High DP-EC values generally indicate fine-grained sediment, while low DP-EC values indicate coarse-grained sediment. Furthermore, hydraulic water pressure and inline pressure offer valuable information on changes in the sediment porosity. The tool consists of a water pump, injecting water at a steady flow rate of ca. 250 mL/min. For more information about DP sensing measurements, see [37,38].

### 3.2. Sediment Coring

In this paper, the focus is laid on 17 sediment cores that were drilled using a Nordmeyer drill rig (RS 0/2.3 Nordmeyer SMAG, Braunschweig, Germany) with a closed auger system. Sediment cores were obtained using dark plastic inliners, each measuring 1 m in length and 5 cm in diameter. Sediment coring and DP logging were carried out on sites at

10 cm distance to obtain comparable datasets. In the laboratory, sediment cores were opened, photographed, and described according to [39]. Sediment samples were taken from different stratigraphic units for further analyses.

### 3.3. Sedimentological Analyses

Grain size analyses were conducted using the pipette and sieving method according to [40]. In total, 1163 samples were analyzed. Additionally, the concentration of organic matter was approximated by loss on ignition (LOI). For this purpose, sediment samples were heated for 2.5 h at 550 °C [41].

X-ray fluorescence (XRF) measurements were carried out on sediment cores by means of a handheld Niton XL3t 900S GOLDD instrument (with calibration mode SOIL; Thermo Fisher Scientific, Waltham, MA, USA) to quantify specific elements. An average measurement interval of 2 cm was selected. In addition, induced coupled plasma-optical emission spectrometry (ICP-OES) analyses were conducted on samples from sediment cores ALP 88A, ALP 89A, ALP 91A, and ALP 92A after extraction using aqua regia (HNO<sub>3</sub> and HCl, 3:1 v/v) in a microwave (Multiwave PRO, Anton Paar, Graz, Austria). For the same cores and using the same analytical instrument, the content of inorganic phosphorous (P) was determined by extraction with H<sub>2</sub>SO<sub>4</sub>, and the content of total P was analyzed using aqua regia [41].

For all cores, magnetic susceptibility was measured using the Bartington MS2 instrument and a MS2K surface sensor (Bartington Instruments Ltd., Witney, UK) with a mean interval of 1 cm. Color measurements were made with a Konica Minolta CM-600d spectrophotometer (Konica Minolta Business Solutions Deutschland GmbH, Langenhagen, Germany) at a mean interval of 1 cm. The color data are given in the CIE-Lab color space. We used a MinMax Scaler to stretch L\* values between 10 and 90 by using the formula  $(L^* - L^*_{\min}) / (L^*_{\max} - L^*_{\min}) \times 80 + 10$  and converted L\*a\*b\* values to RGB color values for enhanced visualization.

Radiocarbon dating was conducted on 26 samples to establish the chronological context of the building structure and its stratigraphic embeddedness. Radiocarbon samples out of charcoal and plant remains were retrieved from sediment cores ALP 88A, ALP 89A, ALP 91A, ALP 92A, and 14C-AMS dated at CEZA Mannheim. We used the Calib REV8.2 software with the IntCal20 calibration curve [42,43] to obtain calibrated ages. Presented radiocarbon ages are given with a standard deviation of 2σ. Further age control was obtained based on archaeological age estimates of numerous diagnostic artifacts found embedded in sediment cores.

### 3.4. Micropalaeontological Analyses

Micropalaeontological investigations focused on ostracods as they provide valuable information on the environmental conditions at the time of sediment deposition and allow conclusions regarding oxygen content, salinity, water depth, and temperature conditions [44–46]. In total, 19 samples taken from sediment cores ALP 88A, ALP 89A, ALP 91A, and ALP 92A (consisting of 15 mL sediment) were analyzed. The samples were divided into three fractions (>400 μm, 400 to >200 μm, 200 to >125 μm) by wet sieving. All samples were counted wet under the stereo microscope (type Nikon SMZ 745 T, Minato, Japan). Taxonomic identification was based on modern determination literature [47–50]. Where possible, individuals were identified to the species level.

### 3.5. Analyses of Vegetation and Fecal Biomarker

The analyses of *n*-alkanes, Δ<sup>5</sup>-sterols, stanols, stanones, and secondary bile acids followed the method of [51] with minor modifications. For Soxhlet extraction, 2–5 g of milled sediment samples were weighed into 23 × 100 mm fiberglass thimbles (Macherey Nagel, Düren, Germany) and covered by a thin layer of quartz sand. Extraction was

performed in 100 mL extractors with 210 mL of dichloromethane/methanol (DCM:MeOH, 2:1, *v/v*) for 36 h. After extraction, internal standards (IS1) *n*-hexatriacontane, 5 $\alpha$ -pregnan-3-one, cholest-5-en-3 $\beta$ -ol-d7, 5 $\alpha$ -cholestan-3 $\beta$ -ol-d5, isodeoxycholic acid, and lithocholic acid-d4 were added to the total lipid extract (TLE). Solutions were concentrated under reduced pressure and completely dried under a gentle stream of nitrogen. TLE was saponified at room temperature for 12–14 h using 3.5 mL of 0.7 M potassium hydroxide in MeOH. A liquid-liquid extraction was carried out to separate *n*-alkanes and  $\Delta$ 5-sterols, stanols, and stanones from secondary bile acids using 10 mL of water and 15 mL of chloroform (CHCl<sub>3</sub>). For separation of bile acids, 6 M HCl (pH < 2) was added to the extract. A solid phase extraction (SPE) was performed to separate *n*-alkanes (eluted with 2  $\times$  2 mL of hexane) and  $\Delta$ 5-sterols, stanols, stanones (eluted with 3 mL of DCM and 2 mL of DCM:acetone (2:1, *v/v*) using PE columns (1 mL) packed with 5% deactivated silica gel (50 mm, mesh: 70–230, pore size: 100 Å, Polygoprep, Macherey Nagel, Germany).

Carboxyl groups of bile acids were methylated with 1.25 M HCl in MeOH at 80 °C for 2 h, and bile acids were purified with SPE using PE columns packed with activated silica gel.  $\Delta$ 5-sterols, stanols, and stanones were silylated with a mixture of *N,O*-Bis(trimethylsilyl)trifluoroacetamide (BSTFA) (containing 1% trimethylchlorosilane, 99:1, *v/v*) and pyridine (3:1, *v/v*) at 90 °C for 1 h. Bile acids were silylated with a mixture of BSTFA (containing 2% trimethylsilylimidazole, 98:2, *v/v*) at 80 °C for 1 h. 5 $\alpha$ -cholestan-3 $\beta$ -ol-d4 was added as IS2 to all samples before analysis.

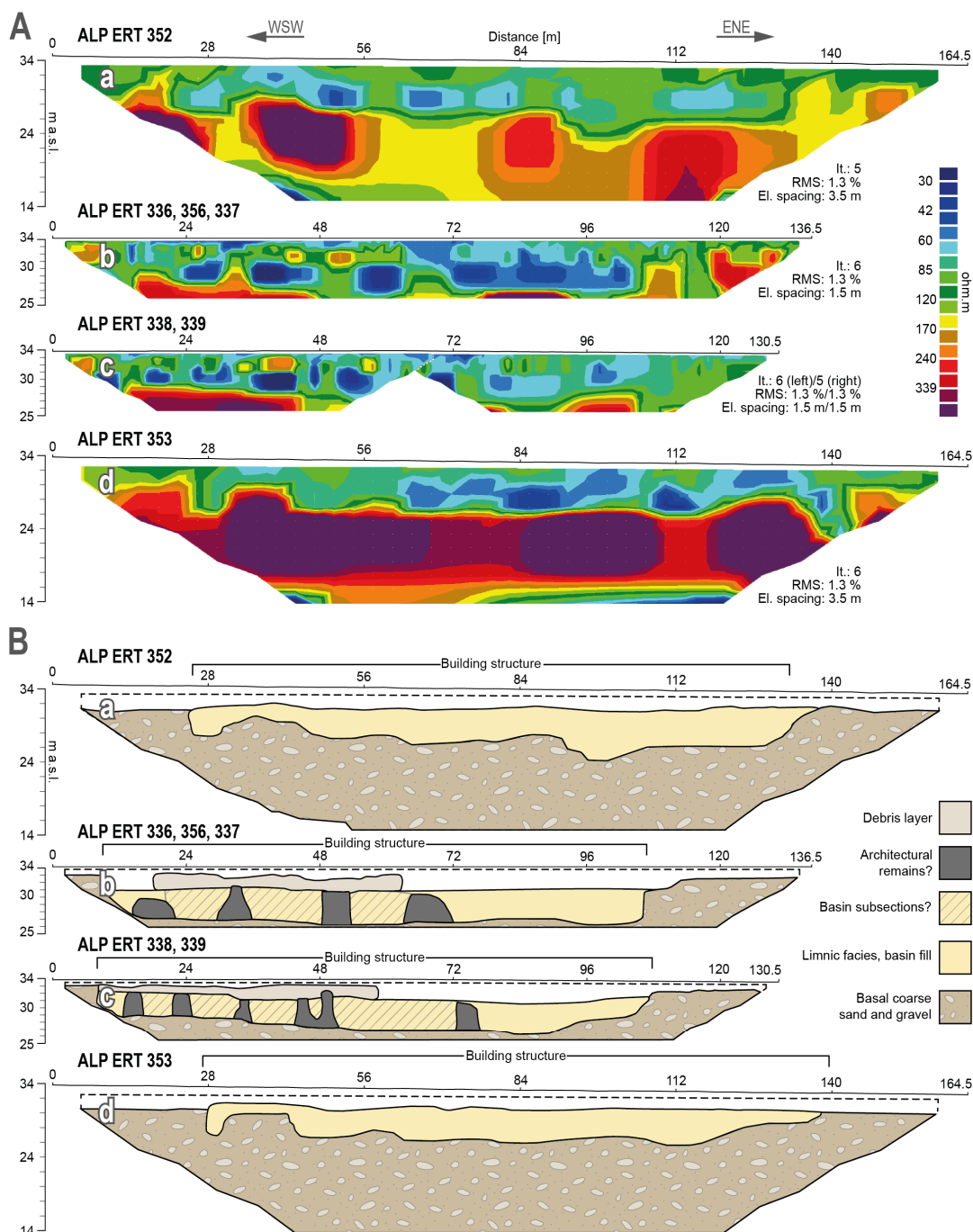
Quantification of *n*-alkanes was conducted via flame ionization gas chromatography (GC-FID, 7890B G3440B, column DB5 MS UI, 30 m  $\times$  0.250 mm  $\times$  0.25  $\mu$ m, Agilent, Santa Clara, CA, USA). H<sub>2</sub> (99.9999%) was used as carrier gas (flow rate 1.5 mL min<sup>-1</sup>). The injection port (split/splitless) was set to 300 °C, and a 1  $\mu$ L sample was injected in splitless mode. The oven temperature program was 80 °C (held 1.5 min) to 300 °C at 5 °C min<sup>-1</sup> (held 20 min). The detector temperature was set to 300 °C.  $\Delta$ 5-sterols, stanols, stanones, and secondary bile acids were analyzed using a 7890B/7000D GC-QQQ-MS system equipped with a DB5-ms Ultra Inert column (30 m  $\times$  0.25 mm  $\times$  0.25  $\mu$ m film thickness, Agilent Technologies, Santa Clara, CA, USA). Data were acquired in selected ion monitoring (SIM) mode for quantification and in scan mode to verify peak identification. He (99.9999% purity) was used as carrier gas (flow rate 1 mL min<sup>-1</sup>). The injection port (split/splitless) was set to 250 °C, and a 1  $\mu$ L sample was injected in splitless mode (1 min splitless time). The oven temperature program was 80 °C (held 1.5 min) to 260 °C at 12 °C min<sup>-1</sup>, to 274 °C at 0.5 °C min<sup>-1</sup>, and to 300 °C (held 10 min) at 10 °C min<sup>-1</sup>. The transfer line temperature was set to 250 °C, the ion source temperature was set to 230 °C, and the MS1/MS2 quadrupole temperature was set to 150 °C.

## 4. Results

### 4.1. Electrical Resistivity Tomography Transects

The ERT transects ALP ERT 352 and ALP ERT 353 (a and d in Figures 1 and 2; both with 3.5 m electrode spacing) show considerable lateral and vertical differences in resistivities. From the ground surface down to approximately 6 m b.s. (m below ground surface) or approximately 28 m above sea level (m a.s.l.), resistivities range between 16 and  $-84.9 \Omega$ m, suggesting a fine-grained substrate. Below this depth, the resistivities increase abruptly ( $>403 \Omega$ m), suggesting a significant shift in texture towards coarser grain sizes. In both the western and eastern sections of the transects, two distinct areas with higher resistivity are also evident at shallower depths (starting from approximately 4 m b.s. or 30 m a.s.l.). These areas appear rectangular and several meters wide (approx. 14 m each), but this abrupt lateral change must be interpreted with caution due to the used electrode configuration.

This boundary is also apparent in ERT transects ALP ERT 336 and ALP ERT 337 (Figure 2). However, resistivity decreases at a depth of 17.4 m b.s.



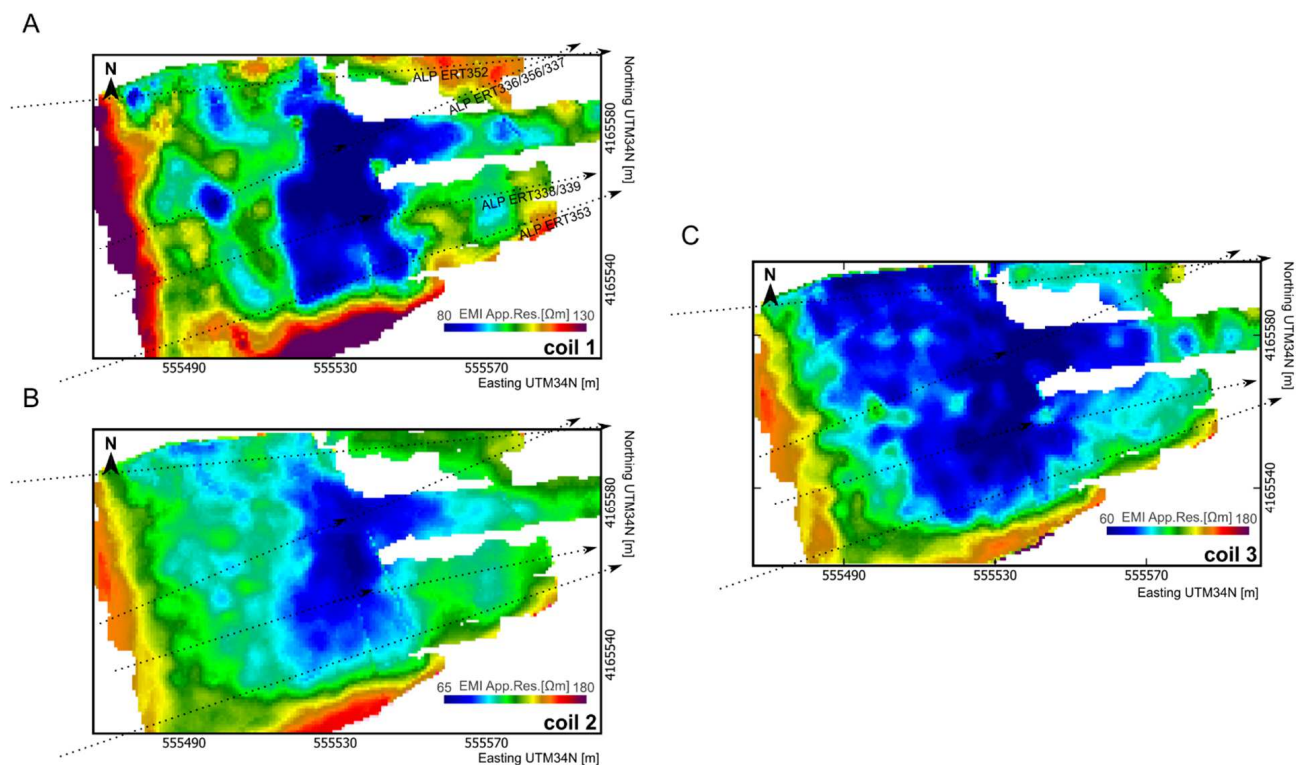
**Figure 2.** Results and schematic interpretation of ERT measurements conducted to the immediate south of the excavated part of ancient Olympia. **(A)** (a,d) Depth sections with 3.5 m electrode spacing. (b,c) Depth sections with 1.5 m electrode spacing, merged. **(B)** Schematic interpretation of ERT depth sections as shown in **(A)**. (a,d) indicate sharp western and eastern edges of the building structure detected to the south of the Southwest Thermae and its low-resistivity, fine-grained filling (yellow). (b,c) show seemingly regular internal structures (dark gray) that can be easily discerned and were found consistent in many more ERT depth sections not presented in this paper. These potential architectural features may represent wall and chamber candidates. Colluvial and alluvial cover sediments are left white. Dashed line represents ground surface. For location of ERT transects, see Figure 1. Note: It = iteration, RMS = root mean square, El = electrode.



Transects ALP ERT 336–339 and 356 (b and c in Figures 1 and 2; both with 1.5 m electrode spacing) offer a more detailed view of the structure’s infill and overlying sediments. Near the surface, a horizontal layer with low resistivities extending down to approximately 1 m b.s. or 33 m a.s.l. is observed with resistivity values below  $60 \Omega\text{m}$ . Below this layer (down to approximately 2.5 m b.s. or 31.5 m a.s.l.), resistivities increase to a range of 71.4–201  $\Omega\text{m}$ . Clearly demarcated areas with low resistivities appear below approximately 3.5 m b.s. or 30.5 m a.s.l., separated by zones of higher resistivity (71–142  $\Omega\text{m}$ ). These transects also highlight an abrupt shift to high-resistivity values at approximately 6.60 m b.s. or 27.40 m a.s.l.

#### 4.2. Frequency Domain Electromagnetic Induction

Figure 3 shows the apparent resistivity of all three EMI coil distances, i.e., for all three integral investigation depth levels. An approximately 100 m by 80 m area of higher conductive material is most notable in all maps. Coil distances 1 and 2 (Figure 3A,B) show patchy features in the western part of the structure. This area coincides with the area of distinct features in the ERT lines. EMI and ERT results correlate well and, for the first time, give information on the dimension of the entire structure.



**Figure 3.** Results of EMI measurements in the study area south of the Southwest Thermae. (A–C) Apparent resistivity maps of coil distances 1 to 3 (for details, see Section 3.1). EMI data reveal a rectangular structure whose orientation is in line with the Leonidaion and the Southwest Thermae. The resistivity of the sedimentary fill of the structure appears much lower than the resistivity of its immediate surroundings.

#### 4.3. Sediment Core Stratigraphy

We distinguish between six sedimentary units based on the detailed analyses of their sedimentological, geophysical, geochemical, and micropalaeontological characteristics as well as molecular biomarker analyses (Table 1 and Figures 4–8).

**Table 1.** Description of the stratigraphic units encountered in sediment cores drilled within the detected building structure to the south of the Southwest Thermae. Units are differentiated by sedimentological, geophysical, and geochemical proxies. The range of values given is based on average values obtained for all sediment cores. The thickness of units is based on the minimum and maximum extent of individual sequences of each unit. Note: MS = magnetic susceptibility; HPT press = hydraulic profiling tool pressure; DP-EC = direct push-electrical conductivity; OM = organic matter; LOI = loss on ignition.








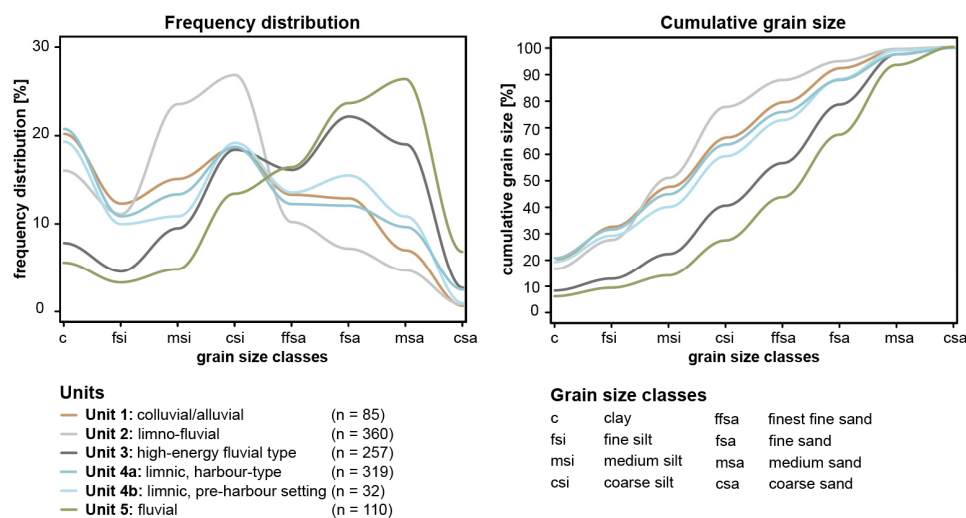
Core Photo	Sedimentary Characteristics	Geophysical Characteristics	Geochemical Characteristics	Thickness
<b>Unit 1: colluvial/alluvial</b>				
	Silt-clay dominated, grey-brown in colour, dark brown topsoil, heavily rooted	Low to high DP-EC values (mean 10.32–48.19 mS/m, overall mean 25.89 mS/m), low to medium HPT press. (mean 23.72–262.77 kPa, overall mean 177.40 kPa)	Low to medium MS (mean $12.03 \times 10^{-5}$ – $28.29 \times 10^{-5}$ ), medium to high content of OM (mean LOI 3.37–5.64%); medium to high Ti/K ratio (mean 0.14–0.20); low to high Zr/Rb ratio (mean 0.71–2.12); Pb values vary from low to medium values (mean 11.31–64.44 ppm), but in most of the sediment cores Pb content is below limit of detection; low to medium P values (mean 373.05–585.81 mg/kg)	Min. thickness 0.25 m, max. thickness 0.76 m, range of 0.51 m
ALP 91A				
<b>Unit 2: limno-fluvial</b>				
	Beige-light brown in colour, partly laminated, contains freshwater gastropods, shows clayey silt intraclasts	Low to high DP-EC values (mean 12.55–44.07 mS/m, overall mean 26.58 mS/m), low to medium HPT press. (mean 34.06–293.35 kPa, overall mean 230.08 kPa)	Low MS (mean $6.98 \times 10^{-5}$ – $12.96 \times 10^{-5}$ ), medium to high content of OM (mean LOI 2.64–4.24%); medium to high Ti/K ratio (mean 0.15–0.17); low to high Zr/Rb ratio (mean 0.48–2.27); low Pb values, (mean 8.99–21.78 ppm); low P values (mean 378.63–409.11 mg/kg)	Min. thickness 0.08 m, max. thickness 1.50 m, range of 1.42 m
ALP 92A				
<b>Unit 3: high-energy fluvial type</b>				
	Silt to fine sand dominated, partly with medium to coarse sand components, beige-light brown in colour, erosional unconformities, poorly sorted	Low to medium DP-EC values (mean 6.24–28.85 mS/m, overall mean 17.11 mS/m), low to medium HPT press. (mean 27.38–262.38 kPa, overall mean 198.75 kPa)	Low MS (mean $4.28 \times 10^{-5}$ – $13.13 \times 10^{-5}$ ); varies from low to medium values in OM (mean LOI 1.43–3.28%); Ti/K ratio varies from medium to high (mean 0.13–0.17); low to high Zr/Rb ratio (mean 0.62–2.50); low to medium Pb values (mean 9.77–56.65 ppm); low P values (mean 207.16–453.02 mg/kg)	Min. thickness 0.01 m, max. thickness 0.96 m, range of 0.95 m
ALP 124A				
<b>Unit 4: limnic, harbour-type</b>				
	Silt-clay dominated, fine-grained, brown-dark brown in colour, partly laminated, contains various charcoal and ceramic remains, contains brick fragments and metal, contains freshwater macrofauna, some sediments	Low to high DP-EC values (mean 8.38–51.65 mS/m, overall mean 34.22 mS/m), low to high HPT press. (mean 29.07–376.53 kPa, overall mean 240.83 kPa)	Medium to high MS (mean $19.91 \times 10^{-5}$ – $99.70 \times 10^{-5}$ ), MS values are highest in this unit within the cores; medium to high OM (mean LOI 2.35–4.21%); medium Ti/K ratio (mean 0.13–0.15); low to medium Zr/Rb ratio (mean 0.63–1.73); Pb varies significantly between sediment cores from low to high values (mean 14.88–90.58 ppm); medium to high P values (mean 863.44–2535.45 mg/kg) indicating strongly eutrophic conditions	Min. thickness 0.02 m, max. thickness 2.58 m, range of 2.56 m
ALP 91A				
<b>Unit 4b: limnic, pre-harbour setting</b>				
	Silt-clay dominated, partly with fine sand components, light brown-brown in colour	Medium DP-EC values (mean 25.18–32.20 mS/m, overall mean 28.04 mS/m), low to medium HPT press. (mean 21.53–278.42 kPa, overall mean 180.49 kPa)	Low to medium MS (mean $9.55 \times 10^{-5}$ – $17.91 \times 10^{-5}$ ) indicating less anthropogenic contamination; medium to high content of OM (mean LOI 2.36–3.77%), medium Ti/K ratio (mean 0.13–0.15); low to high Zr/Rb ratio (mean 0.75–2.11); low Pb values (mean 9.05–14.75 ppm); medium P value (602.61 mg/kg), still indicating eutrophic conditions	Min. thickness 0.33 m, max. thickness 0.93 m, range of 0.60 m
ALP 88A				

Table 1. Cont.

Core Photo	Sedimentary Characteristics	Geophysical Characteristics	Geochemical Characteristics	Thickness
<b>Unit 5: fluvial</b>				
	Fine-to medium sand dominated, gravel, coarse components are visible, varies in colour from shades of brown and grey	Low to medium DP-EC values (mean 1.17–28.85 mS/m, overall mean 11.99 mS/m), low to medium HPT press. (mean 15.73–262.38 kPa, overall mean 182.30 kPa)	Low MS (mean $2.46 \times 10^{-5}$ – $11.11 \times 10^{-5}$ ); low to medium content of OM (mean LOI 1.61–3.22%), low to medium Ti/K ratio (mean 0.10–0.15); low to high Zr/Rb ratio (mean 0.93–2.60); low Pb values (10.40–22.40 ppm), in most of the sediment cores Pb is not detectable; low P values (243.70–335.73 mg/kg)	Min. thickness 0.17 m, max. thickness 1.73 m, range of 1.56 m
ALP 125A				
<b>Unit 6: brick layer</b>				
	Silt to fine sand dominated, partly with medium to coarse sand components, brown-dark brown in colour, contains charcoal and ceramic remains, contains layered bricks and limestone, contains freshwater macrofauna	Low to high DP-EC values (mean 16.26–49.70 mS/m, overall mean 29.82 mS/m), low to high HPT press. (mean 25.82–422.91 kPa, overall mean 217.15 kPa)	Medium to high MS (mean $22.93 \times 10^{-5}$ – $148.04 \times 10^{-5}$ ); low to high content of OM (mean LOI 1.41–4.38%), low to high Ti/K ratio (mean 0.11–0.17); low to high Zr/Rb ratio (mean 0.73–1.39); low to medium Pb values (16.52–52.45 ppm); medium to high P values (mean 895.71–2339.58 mg/kg)	Min. thickness 0.03 m, max. thickness 0.25 m, range of 0.22 m
ALP 92A				

#### 4.3.1. Unit 1: Colluvial/Alluvial

Unit 1 is found in the uppermost section of most sediment cores and represents pedogenically altered colluvial/alluvial sediments (Table 1 and Figures 4–8). The material is dominated by clay and coarse silt and has high organic matter contents (up to 5.6%). Unit 1 material is (dark) brown in color and heavily rooted. Both color and grain size result from soil formation processes. Its thickness between the cores varies from 0.25 to 0.76 m but shows a continuous lateral distribution.



**Figure 4.** Grain size data from 1.163 sediment samples collected from 17 sediment cores drilled in the discovered building structure at ancient Olympia. Results obtained for sediment samples are classified according to sedimentary units 1 to 5 (see Table 1). Left graph shows the mean frequency distribution of grain sizes; right graph shows the mean cumulative grain size based on grain size classes. While units 3 and 5 are sand-dominated, units 1, 2, and 4 are dominated by high silt and clay contents. Area shaded in light blue marks the lateral distribution of unit 4a sediments.

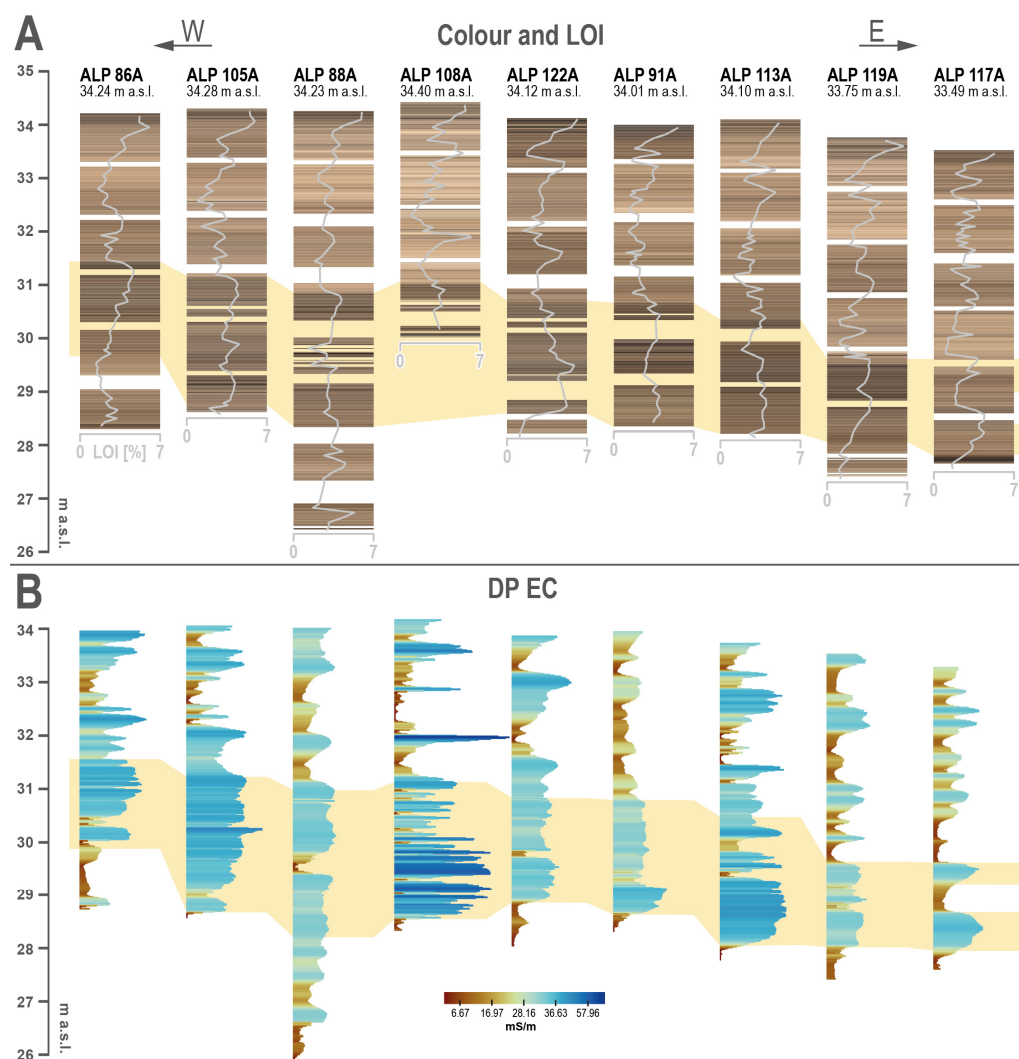
#### 4.3.2. Unit 2: Limno-Fluvial

Unit 2 represents low-energy limno-fluvial depositional conditions (Table 1 and Figures 4–8). The maxima of the frequency distribution are observed for grain size classes clay (16%), medium silt (23.5%), and coarse silt (27%). The sand content is very low. The DP-EC values (up to 44.1 mS/m) are, therefore, significantly increased, and HPT pressure

is decreased. The deposits are laminated and contain freshwater gastropods. The unit occurs adjacent to unit 4 and is interrupted by deposits of unit 3. Due to that, the thickness and frequency of the deposits differ within the different sediment cores. Hence, thickness shows strong variations and ranges from 0.08 to 1.50 m.

#### 4.3.3. Unit 3: High-Energy Fluvial Type (*heft*)

Deposits of unit 3 show a multi-modal grain size distribution with high proportions of coarse silt (18.5%), fine sand (22%), and medium sand (19%; Table 1 and Figures 4–8). The heterogeneous grain size composition results in low DP-EC values and low-medium HPT pressure. Obviously, deposits appear to be poorly sorted. Also, unit 3 often shows an erosional unconformity at its base. In some cores, these deposits also contain fine-grained intraclasts, which indicate an increased flow velocity and erosion of underlying coherent sediments. The alternating deposition of units 2 and 3 suggest successive, sudden changes in the sedimentation process. Units 2 and 3 regularly occur on top of unit 4; however, these deposits may also sporadically interrupt unit 4 deposits. The thickness of unit 3 varies significantly within the cores from 0.01 m to 0.96 m. Unit 3 represents as high-energy fluvial type (*heft*) deposit caused by extreme events associated with fluvial activity, landslides, or debris flows.



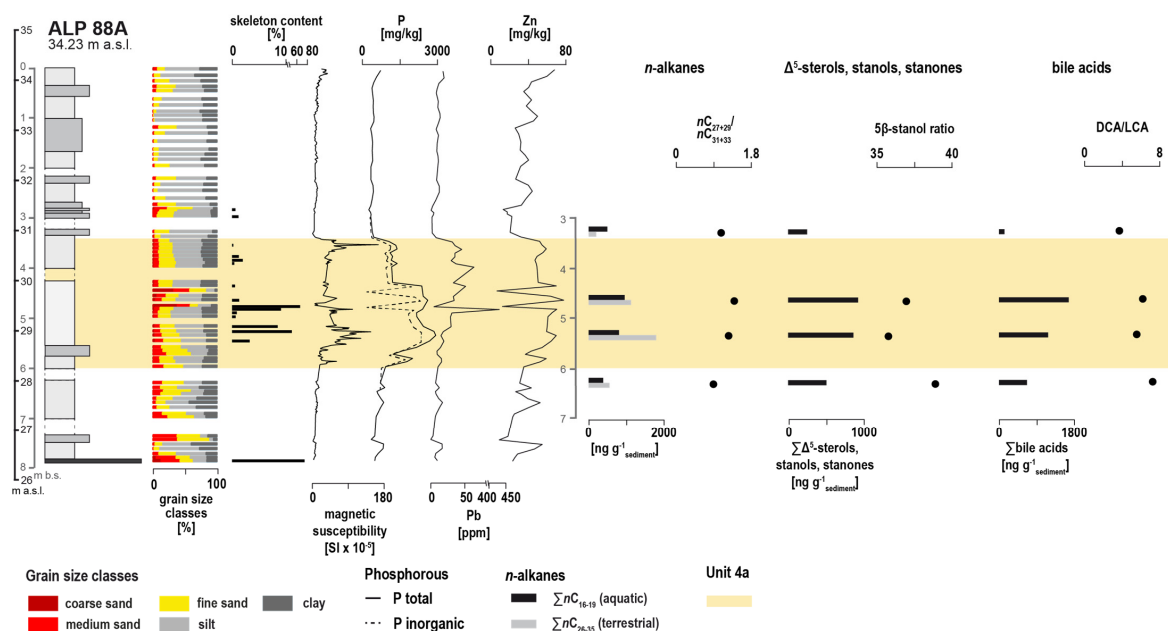
**Figure 5.** Sediment color (RGB) of selected sediment cores drilled along a transect across the detected building structure at Olympia along with LOI values and normalized (dimensionless) electrical conductivity (EC) values measured by direct push-sensing. For location of coring sites, see Figure 1.

DP-EC values were measured in situ using a direct push OIP probe. (A) Sediments of unit 4a show a strikingly dark brown to brown color and are rich in organic matter. (B) DP-EC values were depicted according to a brown-blue color scale and as curve. Brown colors show sections with predominant gravel and sand; blue colors indicate sections with predominant silts and clay. Limnic deposits of unit 4a are shaded in light yellow.

#### 4.3.4. Unit 4: Limnic

Unit 4 reflects low-energy, limnic conditions and is subdivided into subunits 4a and 4b based on their ecological characteristics and markers of anthropogenic influence. Both units are fine-grained, rich in clay and coarse silt, and have elevated organic matter contents (up to 4.2%; Table 1 and Figures 4–8). The predominance of fine grain sizes is evidenced by high DP-EC values (max. mean 51.7 mS/m) and increased HPT pressure (max. mean 376.5 kPa). Subunit 4a is characterized by extraordinarily high P concentrations (max. mean value 2535.5 mg/kg). It further contains numerous anthropogenic remains, such as charcoal fragments and various ceramic fragments, which result in a higher skeletal content. Moreover, the subunit differs strongly from the surrounding deposits due to its brown-to-dark brown color. Anthropogenic contamination is also evident from geochemical proxies as values in magnetic susceptibility and zinc (Zn), and lead (Pb) are significantly higher in subunit 4a compared to all other units. Both measures reach their maximum within this subunit.

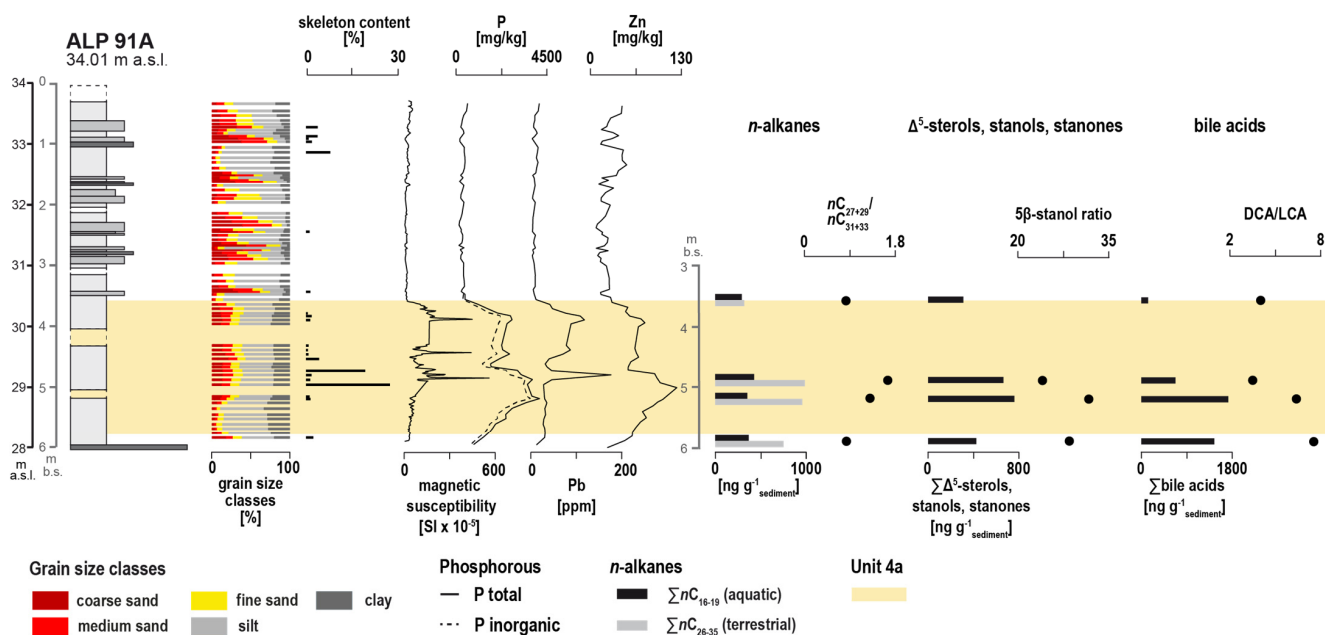
Subunit 4b shows slightly increased P values (max. mean value 602.6 mg/kg). In contrast to subunit 4a, subunit 4b shows no signs of anthropogenic remains, which is supported by low values in magnetic susceptibility and Pb content. Sediments of subunit 4b are light brown to brown in color. The limnic deposits of subunit 4a are relatively thick (up to 2.58 m), with the thickest deposits located in the center of the building structure. They vary in thickness between 0.33–0.93 m. In addition, subunit 4a is present in all cores, whereas subunit 4b is only detected in a few cores immediately below unit 4a (ALP 88A, ALP 117A–120A).



**Figure 6.** Multi-proxy analyses of sediment samples from core ALP 88A showing selected sedimentary, geochemical, and biomarker parameters. The zone shaded in light yellow marks the clay- and silt-dominated fill of the building structure (limnic deposits of unit 4a).  $5\beta$ -stanol ratio stands for  $[5\beta\text{-cholestan-}3\beta\text{-ol}/(5\beta\text{-cholestan-}3\beta\text{-ol} + 5\beta\text{-stigmastan-}3\beta\text{-ol})] * 100$  according to [52]. Note that magnetic susceptibility and P and Pb concentrations are significantly increased in this zone, and, together with n-alkanes, document strong eutrophic conditions.

#### 4.3.5. Unit 5: Fluvial

The grain size distribution of unit 5 deposits is characterized by high contents of fine and medium sand (Table 1 and Figures 4–8). Furthermore, some sediment cores also contain an increased content of gravel. Based on the cumulative grain size curve (Figure 8), this unit represents the coarsest deposit compared to other units recovered from the study area. This is confirmed by low electrical conductivity values (ranging from 1.8 to 28.9 mS/m) and low to medium HPT pressures (ranging from 15.7 to 262.4 kPa) recorded for unit 5. In contrast to unit 4, deposits of unit 5 show low concentrations of P, implying less eutrophic freshwater conditions. Unit 5 was found at the base of most sediment cores, except for cores ALP 91A, ALP 108A, ALP 113A, and ALP 120-122A (probably simply due to their restricted core length). Within the study area, unit 5 deposits are found at significantly shallower depths in the west than in the east. From a geomorphological point of view, this unit documents fluvial processes related to both the Kladeos and the Alpheios rivers. Fluvial deposits encountered in sediment cores ALP 117A and ALP 119A seem to indicate a more pronounced influence by the Alpheios River.



**Figure 7.** Multi-proxy analyses of sediment samples from core ALP 91A showing selected sedimentary, geochemical, and biomarker parameters. The zone shaded in light yellow marks the clay- and silt-dominated fill of the building structure (limnic deposits of unit 4a). 5 $\beta$ -stanol ratio stands for [5 $\beta$ -cholestan-3 $\beta$ -ol]/(5 $\beta$ -cholestan-3 $\beta$ -ol + 5 $\beta$ -stigmastan-3 $\beta$ -ol) \* 100 according to [52]. Note that magnetic susceptibility and P and Pb concentrations are significantly increased in this zone, and, together with n-alkanes, document strong eutrophic conditions.

#### 4.3.6. Unit 6: Stone/Brick Layer

This unit consists of building stones such as shell limestone and tiles that are embedded in a fine-grained matrix (Table 1 and Figures 4–8). Apart from core ALP 124A, unit 6 only intersects unit 4a or appears at its base. Due to the large size of the anthropogenic remains encountered, they may represent remnants of building structures.

#### 4.4. Radiocarbon Dating

Table 2 summarizes the results of radiocarbon-dated samples collected from sediment cores ALP 88A, ALP 89A, ALP 91A, and ALP 92A. All samples were taken from unit 4 with radiocarbon ages ranging from 724–401 cal BC to 343–567 cal AD, thus covering a time

span of over 800 years. All sediment cores show similar radiocarbon ages at comparable depths. Chronostratigraphies are discussed in detail in Section 5.

**Table 2.** AMS radiocarbon analysis of samples from sediment cores ALP 88A, ALP 89A, ALP 91A and ALP 92A. Calibration is based on the Calib 8.2 software with calibration curve IntCal 20 ([42,43]). Note: m a.s.l. = meters above sea level; m b.s. = meter below surface; “;” = several possible age intersections with calibration curve.

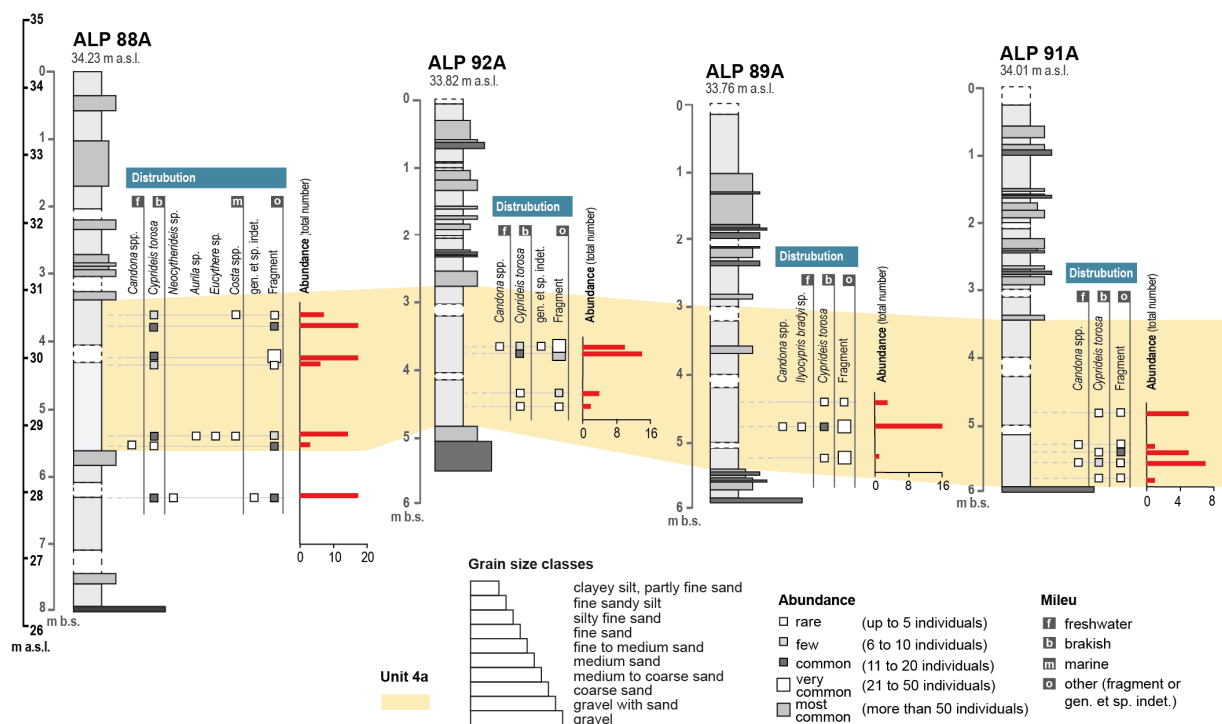
Sample Name	Lab No.	Depth (m b.s)	Depth (m a.s.l.)	Material	14C age BP	+/-	$\delta^{13}\text{C}$ [‰]	1 $\sigma$ Max; Min (cal BC/AD)	2 $\sigma$ Max; Min (cal BC/AD)
ALP 88A/30 HK	56668	3.54	30.69	Charcoal	1559	17	-23.2	cal AD 439; 554	cal AD 434; 567
ALP 88A/33 HK2	56669	3.77	30.46	Charcoal	1787	17	-18.1	cal AD 239; 318	cal AD 230; 330
ALP 88A/41 HK	56671	4.59	29.64	Charcoal	2152	21	-24.4	cal BC 344; 160	cal BC 350; 58
ALP 88A/43 HK	56672	4.84	29.39	Charcoal	2414	19	-22.8	cal BC 514; 412	cal BC 718; 405
ALP 88A/46 HK	56673	5.20	29.03	Charcoal	2315	19	-18.5	cal BC 399-388	cal BC 406-370
ALP 88A/49 HK	56674	5.47	28.76	Charcoal	2303	24	-18.9	cal BC 400-375	cal BC 405; 233
ALP 88A/54 HK2	56675	5.87	28.36	Charcoal	2409	24	-18.6	cal BC 514; 409	cal BC 724; 401
ALP 88A/63 HK	56676	6.92	27.31	Charcoal	29,830	100	-18.9	cal BC 32504-32298	cal BC 32595-32185
ALP 89A/46 KN/Z	56678	3.76	30	Bone	1726	21	-22.4	cal AD 258; 377	cal AD 251; 405
ALP 89A/49 HK	56679	4.26	29.5	Charcoal	2249	24	-22.9	cal BC 383; 231	cal BC 389; 207
ALP 89A/64 HK/OS	56680	4.50	29.26	Charcoal	2395	24	-19.7	cal BC 511; 404	cal BC 715; 400
ALP 89A/54 HK	56681	4.65	29.11	Charcoal	2168	25	-25.4	cal BC 350; 167	cal BC 356; 108
ALP 89A/56 HK	56682	4.86	28.9	Charcoal	2156	27	-27.9	cal BC 348; 124	cal BC 353; 57
ALP 89A/59 HK	56683	5.18	28.58	Charcoal	2313	24	-22.5	cal BC 401-384	cal BC 408; 234
ALP 91A/52 HK	56684	3.76	30.25	Charcoal	1981	26	-27.0	cal BC 32; cal AD 72	cal BC 41; cal AD 118
ALP 91A/53 HK	56685	3.82	30.19	Charcoal	3041	23	-24.9	cal BC 1381; 1260	cal BC 1393; 1220
ALP 91A/54 HK	56686	3.92	30.09	Charcoal	2187	26	-32.5	cal BC 352; 177	cal BC 361; 167
ALP 91A/58 HK	56687	4.44	29.57	Charcoal	2066	22	-22.7	cal BC 104; cal AD 0	cal BC 161; cal AD 6
ALP 91A/62 HK	56688	4.75	29.26	Charcoal	2130	24	-27.0	cal BC 196; 60	cal BC 343; 53
ALP 91A/64 HK	56689	4.87	29.14	Charcoal	2229	24	-22.4	cal BC 364; 208	cal BC 384; 202
ALP 91A/70 HK	56690	5.48	28.53	Charcoal	2250	23	-23.4	cal BC 384; 231	cal BC 389; 207
ALP 91A/71 HK	56691	5.54	28.47	Charcoal	2230	22	-26.6	cal BC 365; 208	cal BC 382; 203
ALP 91A/73 HK	56692	5.72	28.29	Charcoal	2291	22	-21.4	cal BC 397-364	cal BC 401; 232
ALP 92A/38 HK	56693	3.38	30.44	Charcoal	1662	23	-20.5	cal AD 377-424	cal AD 262; 529
ALP 92A/48 HK	56694	4.70	29.12	Charcoal	2118	21	-22.2	cal BC 171; 59	cal BC 335; 52
ALP 92A/49 PR/W	56695	4.78	29.04	Plant fragment	396	20	-25.7	cal AD 1452-1489	cal AD 1446; 1618

#### 4.5. Micropalaeontological Analyses

Micropalaeontological analyses were carried out on 19 samples collected from unit 4. Samples are generally characterized by a low abundance and diversity of ostracods (Figure 8). The total number of species varies between 1 and 17 individuals per sample. The lowest number of individuals per sample was observed in sediment core ALP 89A, whereas the highest number of individuals was found in sediment core ALP 88A.

The ostracod assemblage is predominantly composed of *Cyprideis torosa*, a species typical of brackish environments but which is also common under freshwater conditions [48,49,53]. *Cyprideis torosa* prefers shallow waters near the shoreline with muddy and sandy substrates [48,54]. Under high salinity and/or low-oxygen conditions, this species may occur monospecifically and then indicate strong eutrophication [54,55]. We also identified few individuals exhibiting noded valves, indicating low salinity values during limnic conditions [49,53]. Freshwater species such as *Candona* spp. and *Ilyocypris bradyi* occur

occasionally but only in small numbers. *Candona* spp. and *Ilyocypris bradyi* are common in slowly flowing or standing water as present under limnic environments [48,49]. Both species prefer low salinities [48,49].



**Figure 8.** Results of micropalaeontological analyses of samples from sediment cores ALP 88A, ALP 89A, ALP 91A, and ALP 92A. Encountered ostracod species are classified into different ecological indicator groups. Samples are dominated by the species *Cyprideis torosa* indicating strong eutrophic conditions. The zone shaded in light yellow depicts clay- and silt-dominated sediments of limnic deposits (unit 4a) found within the building structure.

In sediment core ALP 88A, a small number of marine species (i.e., *Neocytherideis* sp., *Aurila* sp., *Eucythere* sp., *Costa* spp.) appear in two samples, possibly brought in by birds. All samples show a high number of ostracod fragments.

#### 4.6. Biomarker Analysis

Sediment cores ALP 88A and ALP 91A (Figures 6 and 7) were chosen for vegetation and fecal biomarker analysis, as they are located inside the unknown building structure and because the related limnic facies (unit 4a) revealed an elevated concentration of P (up to  $>4000 \text{ mg kg}^{-1}$ ). Reference samples were taken from over- and underlying units. An overview of specific analyzed substances (*n*-alkanes,  $\Delta 5$ -sterols, stanols, stanones, and secondary bile acids) and ratios is provided in Figures 6 and 8.

The sums of *n*-alkanes of aquatic origin (*n*C16–*n*C19) varied between 395 and 955  $\text{ng g}^{-1}$  sediment in core ALP 88A and between 292 and 429  $\text{ng g}^{-1}$  sediment in core ALP 91A. The sums of *n*-alkanes derived from terrestrial vegetation (*n*C26–*n*C35) showed concentrations between 200 and 1791  $\text{ng g}^{-1}$  sediment in core ALP 88A and between 320 and 987  $\text{ng g}^{-1}$  sediment in core ALP 91A. The *n*-alkane ratio used for differentiation between open grassland vegetation and mixed deciduous forests ( $n\text{C}27 + n\text{C}29/n\text{C}31 + n\text{C}33$ ) ranged from 0.8 to 1.6, with higher values in unit 4a in both cores.

The sums of  $\Delta 5$ -sterols, stanols, and stanones varied between 252 and 929  $\text{ng g}^{-1}$  sediment in core ALP 88A and between 310 and 758  $\text{ng g}^{-1}$  sediment in core ALP 91A. The ratio  $[5\beta\text{-cholestan-}3\beta\text{-ol}/(5\beta\text{-cholestan-}3\beta\text{-ol} + 5\beta\text{-stigmastan-}3\beta\text{-ol})] \times 100$ , which is



used to distinguish between herbivorous and omnivorous fecal matter, ranged from 24.0 to 38.6% in both cores. The sums of bile acids varied between 133 and 1666 ng g<sup>-1</sup> sediment in core ALP 88A and between 135 and 1728 ng g<sup>-1</sup> sediment in core ALP 91A. The ratio of deoxycholic acid to lithocholic acid ranges from 3.6 to 7.5.

Taken together, samples from sedimentary unit 4a showed significantly higher biomarker concentrations than samples from over- and below-lying facies. In core ALP 88A, biomarker concentrations were significantly higher compared to core ALP 91A. Only the bile acid concentrations were indifferent for both cores.

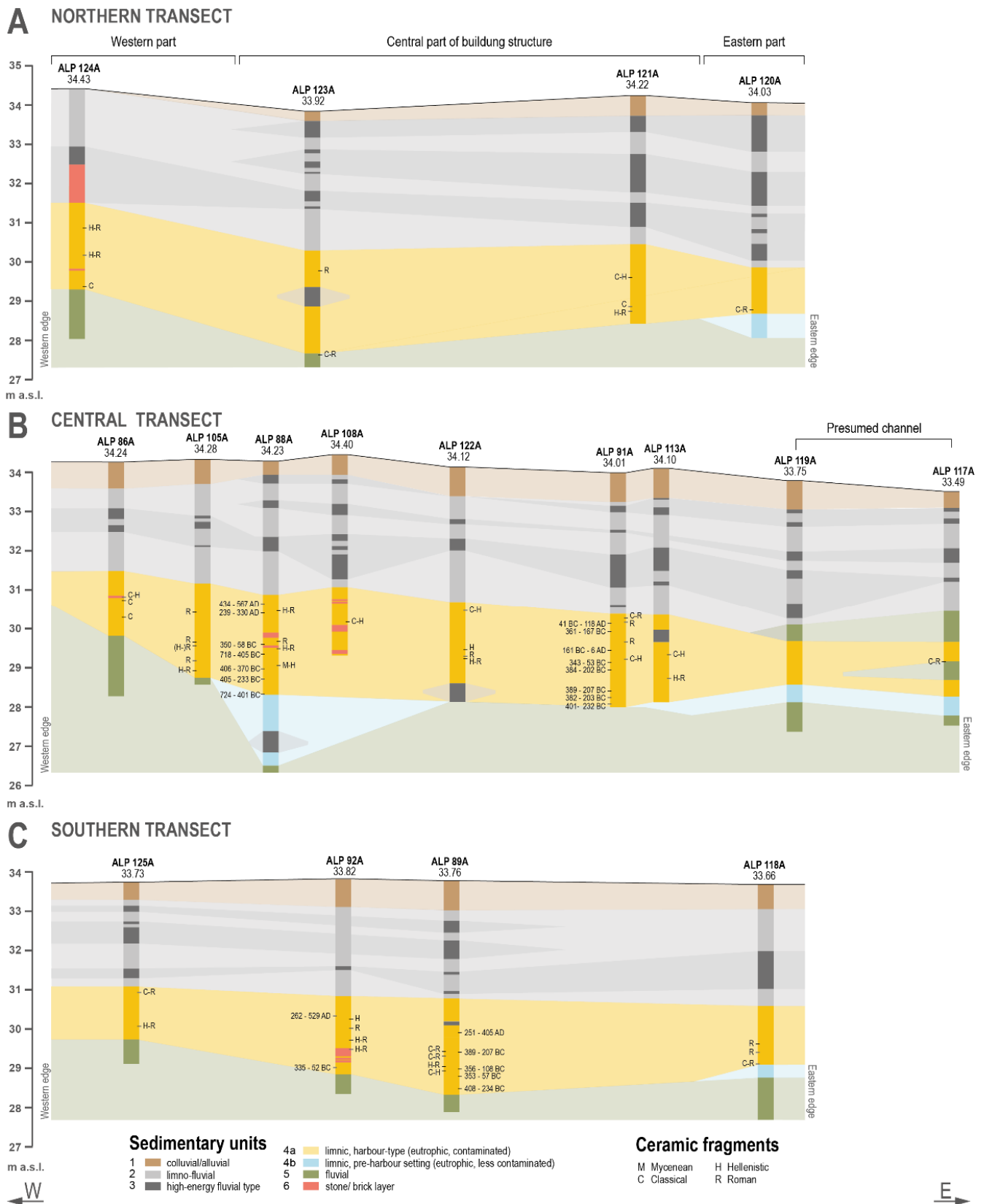
## 5. Discussion

### 5.1. Identification of the Building Structure

As a starting point for the geoarchaeological study presented here, geophysical investigations were carried out to explore local subsurface conditions. The results indicate the existence of an artificial structure, as depicted in Figures 2 and 3. This structure, so far unknown, seems characterized by a rectangular shape, presumably sharp edges, and a fine-grained filling that contrasts sharply with the surrounding material. Its orientation is aligned with excavated buildings such as the Southwest Thermae and the Leonidaion. Moreover, the structure appears to have a flat bottom over most of its width. This strongly suggests that it is of anthropogenic origin and a so far unknown architectural element of ancient Olympia. In terms of dimensions, it spans a length of ca. 100 m (WSW-ENE) and a width of ca. 80 m (NNW-SSE). It seems as if the identified structure is clearly connected to the cult site, and there is an architectural relation with neighboring buildings.

The results of ERT measurements suggest that the building structure is bounded to the west and to the east by high-resistivity building material. The latter is visible as a rectangular shape with sharp outer boundaries (Figure 2). In correlation with the results of EMI measurements, ERT transects also indicate a fine-grained filling of the structure. Moreover, zones of clearly enlarged electrical resistivities encountered in ERT depth sections are considered candidates for man-made structures that demarcate zones with lower resistivities (Figure 2). These results may, therefore, indicate architectural substructures in the western and eastern parts of the building structure.

To sum up, the existence of a building structure to the south of the excavated area of the cult site, still covered by the sediments of the Olympia Terrace, is highly probable. It is known that at least one other building, described as a Roman bath complex, is located to the west of the study area in a comparable geomorphological constellation (Figure 1). Moreover, there are archaeological remnants of a wall made of conglomerates at the edge of the Olympia Terrace, adjacent to the detected building structure. Similar wall remains of this so-called Kladeos Wall can be observed along several hundreds of meters to the northwest of the study area of this paper [56]. Until now, it has been assumed that they continue southward, still covered by the sediments of the Olympia Terrace, and crop out at the Olympia Terrace front (Figure 1). However, our geophysical (ERT, EMI) and, above all, stratigraphic data from cores drilled all over the area of the building structure did not provide any indications of this wall (Figures 2, 3 and 9). Therefore, it can be suggested that the wall that crops out at the Olympia Terrace front may have served another purpose. Consequently, one has to think of a generally different course of the Kladeos Wall than is assumed so far. The function of the wall outcrop itself and its relation to the newly detected building structure remains, however, unclear.



**Figure 9.** Overview of stratigraphic patterns found within the detected building structure to the immediate south of the Southwest Thermae at ancient Olympia. (A) Northern transect within the building structure based on four sediment cores. The thickest layer of limnic, harbor-type sediments (yellow) is observed in the western and central parts of the northern transect. (B) Central transect within the building structure based on nine sediment cores. Results are consistent with (A). Additionally, the high number of ceramic fragments and stone/bricks (red) found in the sediment

cores corroborate the probable existence of a building structure. In the eastern part of the central transect fluvial deposits (green) within the limnic layer of sediment cores ALP 119A and ALP 117A seem to be associated with a channel structure. (C) Southern transect within the building structure based on four sediment cores. Stratigraphic patterns are similar to the ones described for the northern (A) and the central (B) transect. Sedimentological, microfaunal, and geochemical characteristics of sedimentary units 1 to 6 are summarized in Table 1. The zone shaded in light yellow marks limnic unit 4a deposits, which represent the sedimentary fill of the building structure. Based on the results and arguments presented in this paper, we hypothesize that the building structure might have served as a possible inland harbor. Radiocarbon dating indicates that limnic conditions and, thus, the building structure existed at least from the 5th century BC to the 6th century AD. For location of coring sites, see Figure 1.

### 5.2. Stratigraphic Record and Sedimentary Filling of the Building Structure

The fine-grained fill of unit 4a that we identified in 17 sediment cores drilled within the prospected area of the building structure represents a standing water environment of a limnic character. This is evidenced by the predominance of clay and silt and the presence of ostracods, indicating freshwater conditions that are partly highly eutrophic (Figures 4 and 8). These limnic deposits are evident in all the sediment cores retrieved from the building structure and show a total thickness varying between ca. 1.5 m and almost 3 m (Figure 9). In the central part, the limnic sediments were found to be significantly thicker than in the western and eastern parts (Figure 9, central transect). We further observed that the upper boundary of sedimentary unit 4a varies only slightly between 30.5 m to 31.5 m a.s.l. throughout the structure, although the sedimentary surface shows a slight inclination from west to east. The lower boundary of unit 4a shows elevations roughly ranging between 28.5 m and 29.5 m a.s.l. In most cases, unit 4a sediments sit right on top of coarse-grained fluvial deposits (ALP 124A, ALP 123A, ALP 86A, ALP 105A, ALP 91A, ALP 125A, ALP 92A, and ALP 89A; see Figure 9). Overall, the stratigraphic data reveal that the sedimentary fill of the building structure appears to represent an artificial basin with slight inclinations of the unit 4a sediment layer towards the east. At the same time, the basin floor seems to be slightly inclined from both the western and eastern parts towards the central part of the basin. This is also where the deepest sections of the basin were found, namely around coring sites ALP 88A, ALP 122A, ALP 91A, and ALP 113A (Figure 9).

These limnic sediments suggest highly eutrophic conditions, as indicated by several factors. First, limnic deposits of unit 4a exhibit high P concentrations (Figures 6 and 9), which is an indicator of strong eutrophication [57,58]. High P concentrations can be triggered either by natural processes or indicate anthropogenic influence. Anthropogenic eutrophication processes, commonly referred to as cultural eutrophication, are much more rapid. They are mainly caused by the discharge of wastewater and agricultural practices [57,58] and the input of surface water associated with soil erosion processes.

Second, unit 4a reveals a high concentration of fecal lipid markers, which supports the idea of a highly eutrophic sedimentary environment [52]. These markers indicate a combination of fecal inputs from different sources, including humans, cows, sheep, goats, horses, and pigs (Figures 6 and 7). Notably, animal markers found in sediment samples from the building structure outweigh human markers.

Third, such pollution also affects the frequency and distribution of ostracods, with samples showing a decreased abundance [59]. This is evident in our studied samples, as the number of species is consistently low. Additionally, we detected only a small number of typical freshwater species despite assuming low salinity (due to freshwater input from the Alpheios River and the presence of noded individuals of *Cyprideis torosa*). Instead, the species *Cyprideis torosa* dominates, which can also live under reduced oxygen conditions, typical of eutrophic environments resulting from increased primary production [54,55,57].

Based on radiocarbon dating, the limnic, eutrophic conditions found typical of sedimentary unit 4a can be dated to the period between 724–401 cal BC and 343–567 cal AD (Figure 9). This period coincides strikingly with both the beginning and the end of the Panhellenic Games held at Olympia. It is, therefore, reasonable to assume that the onset of eutrophication is associated with the increase in human activities at the ancient site. Similar evidence of strongly increased eutrophication was found on the shore of the Lake of Olympia immediately south of the South Hall [9]. We argue that an increased number of visitors and their supply led to a massive change in ecological conditions. This is supported by identified fecal markers that correspond with bone remains from the Artemis and Pelopion temples [21,24], implying that the high level of pollution of the water body and its sediments probably originates from the cult site. This would also explain why the fecal marker input is higher in the central area of the building (coring site ALP 88A) compared to the southern area of the building (coring site ALP 92A), which is further away from the cult site. Anthropogenic influence is also evident from numerous artifacts embedded within the limnic sediments of unit 4a. These include ceramic fragments (Figure 9) and pieces of charcoal. Strongly increased concentrations of heavy metals (Pb, Zn; Figures 6 and 7) further strengthen the presence of anthropogenically polluted sediments. The very high number of artifacts suggests a distinctly separated building, as we detected significantly fewer artifacts in sediment cores drilled in the immediate vicinity [9]. The strongly increased organic content found associated with unit 4a sediments is reflected in the darker color of the sediment, resulting in a stark contrast with the underlying and overlying sediment layers (Figure 5).

Based on sedimentary, microfaunal, and geochemical data, a lake environment covered large parts of the basins of Makrisia and Ladiko. This Lake of Olympia existed from the 8th millennium BC to at least the 6th century AD [9]. The reconstructed lakeshore was located at ancient Olympia, namely in the immediate environs of the location of the building structure presented in this paper [9]. Considering the fact that the so far unknown building structure described in this paper was obviously filled with water and sediments of a standing water environment, it seems that it formed an architectural connection between the Lake of Olympia on the one hand and the cult site on the other. This is strongly supported by limnic sediments of unit 4b underneath the presumed basis of the building structure with lower P content and without any artifacts in cores ALP 120A, ALP 88A, ALP 119A, ALP 117A, and ALP 118A (Figures 5 and 9). This documents that the limnic environment of the Lake of Olympia must have existed within the area of the later building structure right before its construction.

### *5.3. Interpretation of the Use of the Building Structure*

It has been assumed that the area south of the Altis toward the Alpheios River contained festival grounds that were used by visitors of the Panhellenic Games [1]. This hypothesis has to be reconsidered in the light of geoscientific evidence of the Lake of Olympia [8,9] found right in front of the cult site (Figure 1).

In this paper, we present evidence of a hitherto unknown large building structure immediately south of the Southwest Thermae, which may have served as a link between the cult site and the lake. Based on its structure and analyses of its sediments, we found that the building was continuously filled with water between the 5th century BC and the 6th century AD. Considering these findings against the historical and archaeological background, various possible scenarios can be discussed regarding the function of the building.

### 5.3.1. Scenario 1—Bath Complex

The presence of water within the building suggests that the structure might have been used as a bath complex. It is conceivable that the bath comprised an indoor *thermae* and/or an open-air swimming pool. There is archaeological evidence of several bath complexes at Olympia, including both Greek and Roman baths, such as the Southwest *Thermae*, the South *Thermae*, and the Leonidaion *Thermae* [1,2].

Excavations near the Kladeos River revealed that there was a Greek bathing complex south of the *Palaestra* that also included an open-air swimming pool [50,60–63]. Although large bath complexes with extensive hot and cold-water basins are well-known from the Roman period, such as the Caracalla *Thermae* (220 × 140 m<sup>2</sup>) and the Diocletian's *Thermae* (240 × 140 m<sup>2</sup>) in ancient Rome [62], the bath complexes identified in ancient Olympia are considerably smaller compared to the dimensions of the building structure presented in this paper. For example, the building complex of the Southwestern *Thermae* measures approximately 34 × 43 m<sup>2</sup>. The open-air swimming pool within the Greek bath complex near the Kladeos River measures approximately 24 × 16 m<sup>2</sup> [60].

The idea that the building structure in Olympia represents a large bath complex does also not match the presence of fine-grained sediments in a standing water environment, as the baths would have been supplied with clean freshwater, free of sediments. Even for an outdoor swimming pool, regular cleaning measures of the basin must be expected. Furthermore, the sedimentary infill of the structure documents highly eutrophicated and polluted water conditions, which are not suitable for swimming. Also, numerous findings of ceramic fragments and tiles, as well as other artifacts disposed into the artificial basin, contradict the hypothesis that the building structure was used as a bath complex.

### 5.3.2. Scenario 2—Latrine or Wastewater Basin

The presence of tens of thousands of visitors during the Panhellenic Games meant an immense infrastructural challenge. Not only did people have to be supplied with food and freshwater, but also large amounts of garbage and wastewater had to be managed. Regarding the latter, excavations have so far brought to light archaeological remains of two latrines with capacities for 30 people each, which would not have been sufficient [1]. Based on the highly polluted sediments and the presence of human fecal markers, one might hypothesize that the detected building was used as a latrine and wastewater complex. Several arguments, however, speak against this scenario.

First, a comparison of the fecal marker concentrations with those found in the latrine of Sagalassos in Turkey and other latrines [64] shows that the concentrations of coprostanol in Olympia appear to be far too low (up to 20 times lower). Second, ancient latrines were directly connected to the wastewater system, allowing continuous flushing of human feces underneath the seats to keep the place as clean and hygienic as possible [60,62]. The newly identified building structure presented in this paper is, in contrast, characterized by standing water conditions and, thus, rather represents an artificial basin filled with polluted water. Finally, any wastewater would have been disposed of by the quickest and shortest route directly into the adjacent Lake of Olympia and the Alpheios River that feeds it in order to keep the Olympic cult site free of stench and to minimize the risk of rapidly spreading infectious diseases.

### 5.3.3. Scenario 3—Harbor Installation

Several arguments speak for an interpretation as a possible harbor. The most prominent arguments are that it has a very large size (ca. 8000 m<sup>2</sup>) and, over the entire time of its use (5th century BC until 6th century AD), was filled with water under predominantly limnic conditions. This is proven by fine-grained sediments dominated by clay and silt as

well as by micropalaeontological and geochemical indicators and biomarkers (presence of *n*-alkanes from aquatic vegetation; Figures 6–9).

Moreover, continuous and consistent chronostratigraphies were found all over the structure, showing that it was used as one single unit. The fact that it was constructed at a place where undisturbed pre-existing limnic deposits were encountered—that means in the direct shore area of the Lake of Olympia (Figures 1 and 9)—may indicate that it connected the cult site with the Lake of Olympia. Geophysical and coring results underline that the structure is an artificial basin with its lateral floors gently dipping toward the center where also its deepest parts were found (Figure 9). ERT data further indicate that there are sharp outer edges toward the west and the east and wall candidates, especially in the lateral western part of the structure (Figure 1).

Furthermore, we encountered numerous ceramic fragments as well as fragments of tiles and cooking ware in the sediment cores recovered from the building structure (Figure 9), which may also fit the potential use as a harbor. Ancient harbor basins are known to have been used to dispose of broken goods, and, at the same time, things went overboard during loading and clearing processes, e.g., [65,66].

Also, the strong eutrophication, increased heavy metal concentrations (Figures 6 and 7), and the overall high organic matter content (Figure 5) of the encountered sediments are typical of harbor basins where water exchange was hindered, and some kind of contamination occurred. For example, elevated Pb concentrations were found in the ancient harbors of Kyllini, Lechaion, and Kerkyra [67–69]. Increased Pb contents also serve as a general tracer of anthropogenic activities [65]. According to [70], the daily excretion rate ( $\text{mg day}^{-1}$ ) of an average person is 1400 P, 110 Zn, 3.63 Mg, 3.45 Cu, 0.35 Pb. High Zn concentrations can be interpreted as feces input.

Finally, elevated levels of animal fecal remains might be explained by the transport of animals to Olympia for the supply of food, the clearing of the animal load from ships, and the removal of animal waste in the possible harbor area. Highly polluted conditions were also reconstructed for the area near the South Hall from the beginning of the Panhellenic Games onwards [9], implying that the Riparian zone of the Lake of Olympia near the cult site was highly eutrophic.

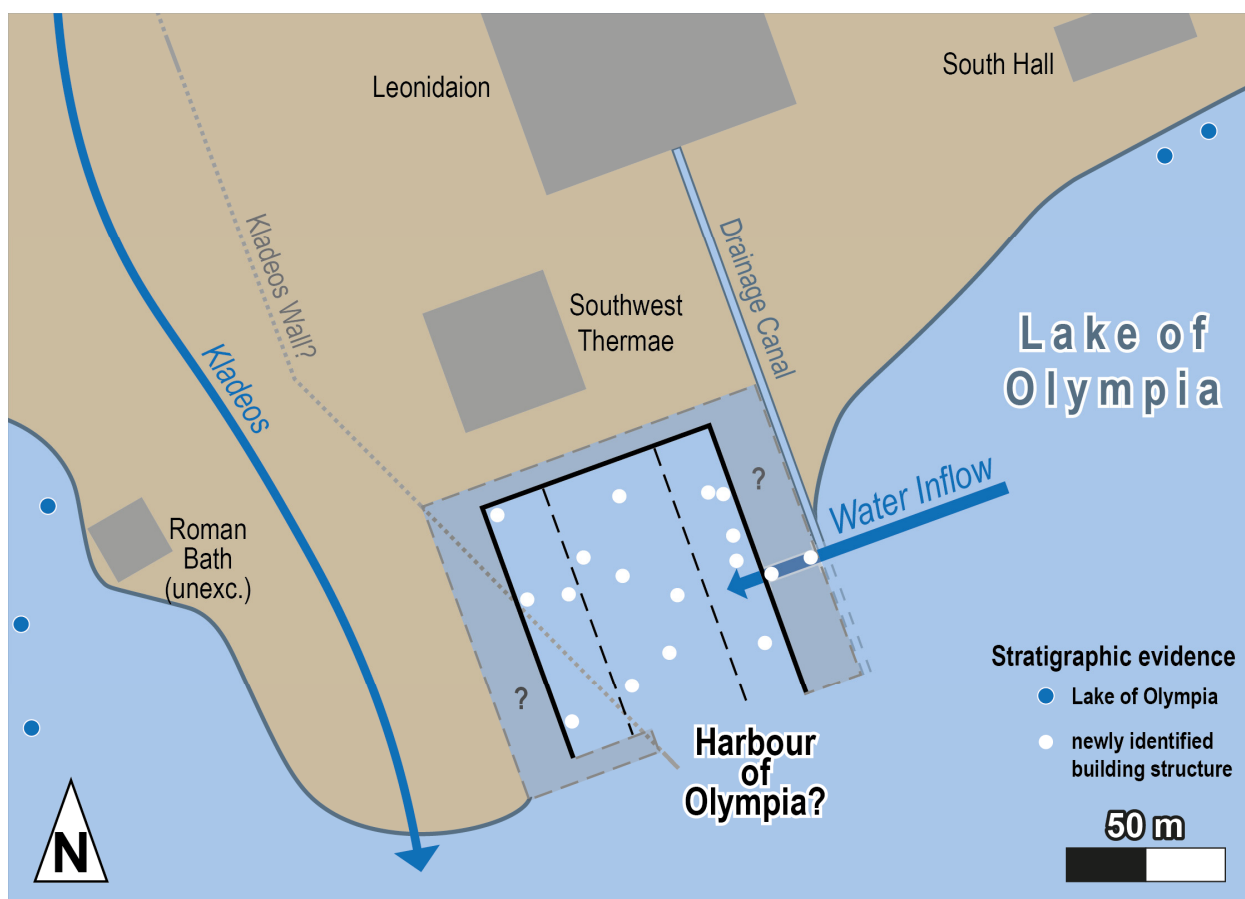
Low-energy conditions, being typical of harbors, explain the general tendency towards strong siltation [65] that can also be observed for the building structure, especially in the second half of the 1st millennium BC (Figure 9). Moreover, the fact that the input of terrestrial plants is higher than that of aquatic plants, as evidenced by the analysis of *n*-alkanes (Figures 6 and 7), documents that considerable amounts of surface water runoff, together with sediments, flowed into the basin. Thus, both water inflow from the cult site and via the nearby Lake of Olympia plus the Alpheios River, feeding it, must be considered. In addition to the characteristic sedimentary filling, both the size and the outline of the structure suggest a possible harbor facility (Figure 10). The outer edges identified in the west and in the east (Figure 2) might represent candidates for former quay walls. The entrance of the possible harbor might have been located to the south of coring sites ALP 92A and ALP 89A, where the basin floor shows the deepest elevations (Figures 9 and 10).

In the eastern part of the building structure, namely to the east of coring sites ALP 117A and ALP 119A (Figures 1, 9 and 10), we documented fluvial sediments interrupting the limnic sequence of unit 4a. Interestingly, these sand layers are also adjusted to the upper edge of the wall candidates identified in the ERT data (Figure 2). We argue that these fluvial sands document the inflow of water into the basin through a canal that opens towards the east, towards the Lake of Olympia, and the lake-feeding Alpheios River (Figure 10). Further ERT data from N-S-running transects measured at the eastern fringe of the building structure, not presented in this paper, underline the presence of such a canal system. In

addition, ERT data suggest an internal architectural subdivision of the building structure (Figure 2). Of course, it is only by archaeological excavations that such questions regarding the building structure and its inner architecture can be verified.

Considering the chronostratigraphic data presented for the building structure (Figure 9), the earliest limnic sediments encountered in cores ALP 88A, ALP 91A, ALP 92A, and ALP 89A are radiocarbon dated to 724–401 cal BC, 401–232 cal BC, 335–52 cal BC and 408–234 cal BC, respectively. Apart from the basal age of 724–401 cal BC found at site ALP 91A which also covers older periods, perhaps due to reworking effects affecting the sample, the basal ages of unit 4a are very consistent and suggest that the building structure was set in use as early as in the Classical period. The radiocarbon-based chronostratigraphy is generally consistent with numerous diagnostic sherds found embedded in unit 4a, although some of the sherds indicate possible reworking effects (Figure 9). Moreover, fragments of limestone and conglomerate found within and below unit 4a deposits indicate that this material was used as the initial building material.

To sum up, among the three scenarios presented, scenario 3 (harbor) fits best with geophysical and geoarchaeological data, in particular with the results of multi-proxy analyses of the sediment fill of the building structure.



**Figure 10.** Schematic sketch of the palaeogeographical situation south of the Southwest Thermae and the Leonidaion with the hypothesized harbor that possibly connected the Lake of Olympia with the cult site mainly based on detailed multi-proxy analyses of sediment cores (white and blue dots). Sediment cores at the eastern fringe of the building structure suggest an inflow of water through a canal from the east (see Figure 9). The solid black line delineates the outline of the building structure and its interpretation as possible harbor based on geoarchaeological evidence. Black dashed lines separate the deepest central part of the presumed harbor structure from the shallower eastern and western parts (see Figure 9). Zones shaded in light gray and surrounded by gray dashed lines in the

immediate vicinity of the building structure represent assumed quay or harbor areas above the waterline. Gray pointed line delineates the presumed course of the Kladeos Wall (excavated sections with solid line), still unearthened, according to the excavation plan of the DAI. The drainage canal of the Leonidaion seems to have flown into the Lake of Olympia right east of the assumed harbor area. Archaeological evidence by excavation for possible harbor infrastructure and road are still pending.

#### 5.4. Final Phase of the Building Structure and Its Sedimentary Burial

As the uppermost samples retrieved from unit 4a from cores ALP 88A, ALP 92A, and ALP 89A yielded radiocarbon ages of 434–567 cal AD, 262–529 cal AD, and 251–401 cal AD, respectively, the building structure seemed to have been in use until the 6th century AD (Figure 9). In each sediment core retrieved from it, harbor-type limnic sediments of unit 4a were found abruptly overlain by light-brownish, beige-colored sands and silts of units 2 and 3 (Figure 9). Within the first 10–15 cm of sediments found on top of brown-to-dark-brown colored unit 4a deposits, however, the predominant grain size remains clayey silt, documenting that the building still functioned as a water collection basin for a short time after it was out of use. At the same time, organic matter enrichment and eutrophication seemed strongly diminished (Figures 5 and 9). Presumably within a few decades after its final use, the site was then buried underneath a thick sequence of alternating (limno-)fluvial, silty sediments and high-energy sands (Figure 9, Table 2).

Sediments of the first high-energy event layer covering the building structure, were already described and dated by [9] from the area immediately west of it (ALP 5, ALP 83A) and south of the South Hall (ALP 66A, ALP 67A; see Figure 1), and are also found in core stratigraphies from the building structure itself. They can be confined to the period between 424–538 cal AD and 596–647 cal AD [9]. Thus, the youngest radiocarbon date documenting the building still in use is 434–567 cal AD (Figure 9), while the high-energy event that let it disappear under a thick cover out of sands and silt (event 5 of [9]) occurred at or after 596–647 cal AD. This last age fits very well with the archaeological evidence for the last settlement activities found at the cult site, which date to the second half of the 7th century AD [22,23]. These settlement activities were obviously stopped by the high-energy event. It is under discussion whether the corresponding event was triggered by a large earthquake that happened around 521 AD/551 AD [71–73] and had destructive effects on Olympia [9,74].

We assume that it was not the earthquake as such that destroyed Olympia and the detected building structure but that there were tremendous secondary effects triggered by the earthquake that created the event layer described above. We argue that earthquake-induced landslides in the marly bedrock of the Kladeos Valley led to a complete blocking of the valley and the formation of temporary lakes. Corresponding sediments were found in sediment cores in the entire Kladeos Valley, currently being prepared for publication by our interdisciplinary working group. The general geomorphodynamic mechanism and related processes at Olympia were already identified in the first half of the 20th century [75]. The bursting of such earthquake-triggered, landslide-dammed lakes in the Kladeos Valley resulted in severe flooding of the ancient site by *heft* events and mudflows. With regard to the building structure interpreted as a harbor, this hypothesis is supported by findings of a consistent *heft* layer in many cores showing a clear inclination from northwest to southeast in the northern, central, and southern parts of the building structure (Figure 9). This suggests that the *heft* layer entered the building structure from the northwest, which, in turn, implies that it originated from the Kladeos Valley. On the base of the above-discussed data, one may finally hypothesize that the earthquake caused the end of the use of the building structure shortly after a point of time between 434–567 cal AD. Both earthquakes of 521 and 551 AD can, therefore, be considered as possible triggering events. Over the following decades, landslide-dammed lakes continuously filled with Kladeos waters and



finally broke to bury Olympia and its harbor under *heft* and mudflow deposits. This must have happened at or shortly after 596–647 cal AD.

### 5.5. (Geo-)Archaeological Implications

The existence of a possible harbor facility south of the ancient site would have a variety of (geo-)archaeological implications. A harbor would represent a relevant link between the ancient site and the Lake of Olympia, which existed from the 8th millennium BC at least until the 6th century AD (Figure 10). This, in turn, would infer that the lake could have been used as a waterway to the ancient site and may have served to clear building material and any kind of wares and to supply the visitors of the cult site with food. It is further conceivable that the harbor would have also been used to dispose of wastewater collected on the site and/or dirt water from cleaning wares in the harbor area. Disembarking of livestock and harbor-near slaughtering might explain the high eutrophication, high concentrations of heavy metals, and increased fecal lipid markers found in harbor sediments. Despite the geoarchaeological evidence and many arguments presented in this paper suggesting that the newly identified building structure might represent an inland harbor at the southern edge of ancient Olympia, it remains questionable why such an infrastructure is not mentioned in any known written records that describe the cult site. Again, only by archaeological excavation, one will be able to validate the results of our prospective geoarchaeological investigations presented in this paper.

## 6. Conclusions

Based on multi-proxy analyses of sediment cores drilled at the southern edge of the cult site of Olympia, we were able to detect and analyze a previously unknown building structure. Our main findings are as follows:

- (a) The building structure, as suggested by geophysical prospection, measures at least 100 m (WSW-ENE) times 80 m (NNW-SSE). Its outer rectangular structure seems to be in line with the orientation of other buildings of ancient Olympia such as the Leonidaion and the Southwest Thermae. The building structure seems to have distinct outer edges and may be internally subdivided into two lateral sections in the west and the east with architectural structures, and a central basin. Detailed stratigraphic data confirm that the entire structure resembles an artificial basin with a floor that is slightly inclined from both west and east towards the central part. The deepest parts are in the central south section of the structure.
- (b) The building structure is filled with brown-to-dark-brown low-energy sediments of unit 4a dominated by clay and silt and rich in organic matter. Geochemical proxies document strong eutrophication and contamination with heavy metals. Ostracod analyses revealed limnic conditions in a dirty, standing water environment. High concentrations of *n*-alkanes and fecal lipid markers document considerable inflow of surface water and input of human and animal-borne excrements, respectively. Radio-carbon ages show that such limnic conditions persisted from the 5th century BC to the 6th century AD, thus largely covering the period of the Panhellenic Games.
- (c) Regarding the function of the building structure, we hypothesize that it may have served as a possible harbor installation. This interpretation is supported by its size, the materials used, the geoarchaeological interpretation of sediment-based proxies, and its location right between the cult site and the newly discovered Lake of Olympia.
- (d) The identified building stopped being in use shortly after 434–567 cal AD when the latest harbor-type limnic deposits were accumulated. We hypothesize that its stop of use is related to the impact of catastrophic earthquakes said to have hit Olympia in 521/551 AD. Earthquake-triggered landslides in the Kladeos River valley are assumed

to have dammed up temporary lakes, the dams of which subsequently burst and caused high-energy floods—and mudflows. Their deposits covered the cult site and the identified building structure at or shortly after 596–647 cal AD. This is exactly the time when settlement activity at the cult site of Olympia stopped, based on archaeological evidence.

- (e) The existence of an inland harbor infrastructure that linked the cult site with the Lake of Olympia would entail considerable (geo-)archaeological implications. Among others, the lake could have been used as a waterway to the ancient site and may have served to clear building material or any kind of wares and to supply the visitors of the ancient cult site with food. A conclusive evaluation of the building structure can, of course, only be given by detailed archaeological excavations.

**Author Contributions:** Conceptualization: A.V., L.S., L.O., F.L. and H.-J.G.; methodology: L.S., A.V., L.O., P.F., D.W. and S.B.; validation: L.S., A.V. and L.O.; investigation: L.S., A.V., L.O., E.A., P.F., T.W., S.B. and D.W.; data curation: L.S., L.O., P.F., T.W. and G.P.; writing—original draft: L.S., D.W., S.B., S.S. and S.F.; writing—review and editing: A.V., P.F., D.W., S.B., S.S., S.F., F.L., H.-J.G., B.E., E.-I.K., O.P. and D.W.; visualization: L.S., D.W., S.B., E.A. and B.T.; supervision: A.V. and E.-I.K.; project administration: A.V.; O.P.; fundraising: A.V., B.E., H.-J.G. and F.L. All authors have read and agreed to the published version of the manuscript.

**Funding:** This research is part of the project entitled “Olympia (Greece) as a multi-dimensional space—a landscape archaeology approach to structure, interdependency and change of spatial networks” (project number 270113181) funded by the German Research Foundation (Deutsche Forschungsgemeinschaft, DFG).

**Data Availability Statement:** All basic data as well as new results are accessible via the central project server of Johannes Gutenberg-Universität Mainz in cooperation with the Center for Data Processing at JGU using the following link: <https://seafilerlp.net/d/7ac183077dd64a9b9a93/> (accessed on 15 January 2025).

**Acknowledgments:** Our deepest thanks are addressed to the directorate and the team of the Ephorate of Antiquities of Ilia, namely to Christos Liangouras and Thalia Diamantopoulou, and the directorate and staff of the German Archaeological Institute (Deutsches Archäologisches Institut, Athens), namely to Hakon Rueckemann M.A. and Stefan Biernath, for valuable support during fieldwork and fruitful discussions. Further thanks are due to all involved members of the Natural Hazard Research and Geoarchaeology team and of the Soil Geography group at Mainz, especially to Gerlinde Borngässer, Tina Georg, Tom Haseloer, Felix Henselowsky, Stefanie Klassen and Aileen Klinger for their help during field and laboratory analyses.

**Conflicts of Interest:** The authors declare that they have no known competing financial interests or personal relationships that could have appeared to influence the work reported in this paper.

## References

1. Sinn, U. *Das antike Olympia: Götter, Spiel und Kunst*, 2nd ed.; C.H.Beck: München, Germany, 2004.
2. Heilmeyer, W.-D.; Kaltsas, N.; Gehrke, H.-J.; Hatzi, G.E.; Bocher, S. (Eds.) *Mythos Olympia. Kult und Spiele*; Prestel: München, Germany, 2012.
3. Kyrieleis, H. *Olympia*; Wissenschaftliche Buchgesellschaft: Darmstadt, Germany, 2011.
4. Vött, A. *Neue Geoarchäologische Untersuchungen zur Verschüttung Olympias. Eine Einführung in Die Olympia-Tsunami-Hypothese*; Harrassowitz: Wiesbaden, Germany, 2013.
5. Hoppe, A.; Lehné, R.; Hecht, S.; Vött, A. Olympia im Kontext der jüngsten Erd- und Landschaftsgeschichte. In *Mythos Olympia. Kult und Spiele*; Heilmeyer, W.-D., Kaltsas, N., Gehrke, H.-J., Hatzi, G.E., Bocher, S., Eds.; Prestel: München, Germany, 2012; pp. 232–235.
6. Moustaka, A. Die deutschen und griechischen Ausgrabungen. In *Mythos Olympia. Kult und Spiele*; Heilmeyer, W.-D., Kaltsas, N., Gehrke, H.-J., Hatzi, G.E., Bocher, S., Eds.; Prestel: München, Germany, 2012; pp. 173–179.

7. Schnapp, A. Vergessen und Wiederentdeckung Olympias von den Anfängen bis zur Expedition de Morée. In *Mythos Olympia. Kult und Spiele*; Heilmeyer, W.-D., Kaltsas, N., Gehrke, H.-J., Hatzi, G.E., Bocher, S., Eds.; Prestel: München, Germany, 2012; pp. 159–165.
8. Slabon, L.; Obrocki, L.; Fischer, P.; Willershäuser, T.; Lang, F.; Gehrke, H.-J.; Eder, B.; Kolia, E.-I.; Pilz, O.; Wilken, D.; et al. The “Lake of Olympia”: Geoarchaeological evidence of a lake environment in the vicinity of ancient Olympia (western Peloponnese, Greece). In *Advances in On- and Offshore Archaeological Propection, Proceedings of the 15th International Conference on Archaeological Propection, Kiel, Germany, 28 March–1 April 2023*; Wunderlich, T., Hadler, H., Blankenfeldt, R., Eds.; Kiel University Publishing: Kiel, Germany, 2023; pp. 41–50. [\[CrossRef\]](#)
9. Slabon, L.; Obrocki, L.; Bäuml, S.; Eder, B.; Fischer, P.; Gehrke, H.-J.; Kolia, E.-I.; Lang, F.; Pantelidis, G.; Pilz, O.; et al. The Lake of Olympia: Sedimentary evidence of a mid- to late Holocene lake environment in the vicinity of ancient Olympia (western Peloponnese, Greece). *Quat. Environ. Hum.* 2025; *under review*.
10. Kalogeropoulos, K.; Tsanakas, K.; Stathopoulos, N.; Tsemmelis, D.E.; Tsatsaris, A. Cultural heritage in the light of flood hazard: The case of the “Ancient” Olympia, Greece. *Hydrology* 2023, 10, 61. [\[CrossRef\]](#)
11. Institute for Geology and Mineral Exploration (IGME). *Geological Map of Greece, 1:50,000*; Olympia Sheet: Athens, Greece, 1982.
12. Vött, A.; Willershäuser, T.; Röbbke, B.R.; Obrocki, L.; Fischer, P.; Hadler, H.; Emde, K.; Eder, B.; Gehrke, H.-J.; Lang, F. Major flood events recorded in the Holocene sedimentary sequence of the uplifted Ladiko and Makrisia basins near ancient Olympia (western Peloponnese, Greece). *Z. Geomorphol. Suppl. Issues* 2015, 59, 143–195. [\[CrossRef\]](#)
13. Papanikolaou, D.; Fountoulis, I.; Metaxas, C. Active faults, deformation rates and Quaternary paleogeography at Kyparissiakos Gulf (SW Greece) deduced from onshore and offshore data. *Quat. Int.* 2007, 171–172, 14–30. [\[CrossRef\]](#)
14. Vött, A.; Fischer, P.; Röbbke, B.R.; Werner, V.; Emde, K.; Finkler, C.; Hadler, H.; Handl, M.; Ntageretzis, K.; Willershäuser, T. Holocene fan alluviation and terrace formation by repeated tsunami passage at Epitalio near Olympia (Alpheios River valley, Greece). *Z. Geomorphol. Suppl. Issues* 2015, 59, 81–123. [\[CrossRef\]](#)
15. Papadopoulos, G. Historical Seismicity of the Kyparissiakos Gulf, Western Peloponnese, Greece. *Boll. Di Geofis. Teor. Ed Appl.* 2014, 55, 389–404. [\[CrossRef\]](#)
16. Gehrke, H.-J. Einleitung—Olympia in der Geschichte. In *Mythos Olympia. Kult und Spiele*; Heilmeyer, W.-D., Kaltsas, N., Gehrke, H.-J., Hatzi, G.E., Bocher, S., Eds.; Prestel: München, Germany, 2012; pp. 29–35.
17. Kyrieleis, H. Die frühe Geschichte Olympias—Mythos und archäologische Forschung. In *Mythos Olympia. Kult und Spiele*; Heilmeyer, W.-D., Kaltsas, N., Gehrke, H.-J., Hatzi, G.E., Bocher, S., Eds.; Prestel: München, Germany, 2012; pp. 61–65.
18. Kyrieleis, H. *Anfänge und Frühzeit des Heiligtums von Olympia. Die Ausgrabungen am Pelopion 1987–1996*; Olympische Forschungen, vol. 31; De Gruyter: Berlin, Germany, 2006.
19. Mallwitz, A. *XI. Bericht über die Ausgrabungen in Olympia*; De Gruyter: Berlin, Germany, 1999.
20. Sinn, U. Olympia und die Spiele in römischer Zeit. In *Mythos Olympia. Kult und Spiele*; Heilmeyer, W.-D., Kaltsas, N., Gehrke, H.-J., Hatzi, G.E., Bocher, S., Eds.; Prestel: München, Germany, 2012; pp. 105–109.
21. Barringer, J.M. *Olympia: A Cultural History*; Princeton University Press: Princeton, NJ, USA, 2021.
22. Völling, T.; Baitinger, H.; Ladstätter, S.; Rettner, A. Olympia in frühbyzantinischer Zeit. Siedlung—Landwirtschaftliches Gerät—Grabfunde—Spolienmauer. In *Olympische Forschungen Vol. 34*; iDAI Publications/Books: Berlin, Germany, 2023. [\[CrossRef\]](#)
23. Mallwitz, A.; Schering, W. Die Werkstatt des Pheidias in Olympia. Erster Teil. In *Olympische Forschungen*; De Gruyter: Berlin, Germany, 1964; Volume 5.
24. Heiden, J. Artemis-Altäre. In *Mythos Olympia. Kult und Spiele*; Heilmeyer, W.-D., Kaltsas, N., Gehrke, H.-J., Hatzi, G.E., Bocher, S., Eds.; Prestel: München, Germany, 2012; pp. 145–147.
25. Wunderlich, T.; Wilken, D.; Erkul, E.; Rabbel, W.; Vött, A.; Fischer, P.; Hadler, H.; Heinzmann, M. The river harbour of Ostia Antica—Stratigraphy, extent and harbour infrastructure from combined geophysical measurements and drillings. *Quat. Int.* 2018, 473, 55–65. [\[CrossRef\]](#)
26. Giaime, M.; Jol, H.M.; Salmon, Y.; López, G.I.; Abu Hamid, A.; Bergevin, L.; Bauman, P.; McClymont, A.; Sailer-Haugland, E.; Artzy, M. Using a multi-proxy approach to locate the elusive Phoenician/Persian anchorage of Tel Akko (Israel). *Quat. Int.* 2021, 602, 66–81. [\[CrossRef\]](#)
27. Kirchner, A.; Zielhofer, C.; Werther, L.; Schneider, M.; Linzen, S.; Wilken, D.; Wunderlich, T.; Rabbel, W.; Meyer, C.; Schmidt, J.; et al. A multidisciplinary approach in wetland geoarchaeology: Survey of the missing southern canal connection of the Fossa Carolina (SW Germany). *Quat. Int.* 2018, 473, 3–20. [\[CrossRef\]](#)
28. Siart, C.; Ghilardi, M.; Forbriger, M.; Theodorakopoulou, K. Terrestrial laser scanning and electrical resistivity tomography as combined tools for the geoarchaeological study of the Kritsa-Latô dolines (Mirambello, Crete, Greece). *Géomorphologie Relief Processus Environ.* 2012, 18, 59–74. [\[CrossRef\]](#)
29. Melis, R.; Borgia, E.; Agostini, S.; Celant, A.; Di Rita, F.; Forte, E.; Salvi, G.; Colizza, E. Palaeoenvironmental evolution and decline of the harbours of the Roman and Early Byzantine city of Elaiussa Sebaste (southeastern Turkey): Natural and anthropic causes. *J. Quat. Sci.* 2024, 40, 153–173. [\[CrossRef\]](#)

30. Ullrich, B.; Meyer, C.; Weller, A. Geoelektrik und Georadar in der archäologischen Forschung: Geophysikalische 3D-Untersuchungen in Munigua (Spanien). In *Einführung in die Archäometrie*; Wagner, G., Ed.; Springer: Berlin/Heidelberg, Germany, 2007; pp. 75–93.
31. Obrocki, L.; Eder, B.; Gehrke, H.-J.; Lang, F.; Vött, A.; Willershäuser, T.; Rusch, K.; Wilken, D.; Hatzi-Spiliopoulou, G.; Kolia, E.-I.; et al. Detection and localization of chamber tombs in the environs of ancient Olympia, Peloponnese, Greece, based on a combination of archaeological survey and geophysical prospection. *Geoarchaeology* **2019**, *34*, 648–660. [[CrossRef](#)]
32. Bäuml, S.; Wilken, D.; Fischer, P.; Obrocki, L.; Slabon, L.; Willershäuser, T.; Eder, B.; Gehrke, H.-J.; Kolia, E.-I.; Lang, F.; et al. The discovery of an unknown structure of the Sanctuary of Olympia by means of geophysical prospection. *PLoS ONE* **2025**, submitted.
33. Loke, M.H.; Barker, R.D. Rapid Least-Squares Inversion of apparent resistivity pseudosections by a quasi-Newton method. *Geophys. Prospect.* **1996**, *44*, 131–152. [[CrossRef](#)]
34. De Smedt, P.; Van Meirvenne, M.; Saey, T.; Baldwin, E.; Gaffney, C.; Gaffney, V. Unveiling the prehistoric landscape at Stonehenge through multi-receiver EMI. *J. Archaeol. Sci.* **2014**, *50*, 16–23. [[CrossRef](#)]
35. Nabighian, M. *Electromagnetic Methods in Applied Geophysics*; Application; Society of Exploration Geophysicist: Oklahoma, OK, USA, 1991; Volume 2.
36. Wilken, D.; Mercker, M.; Fischer, P.; Vött, A.; Erkul, E.; Corradini, E.; Pickartz, N. Artificial bee colony algorithm with adaptive parameter space dimension: A promising tool for geophysical electromagnetic induction inversion. *Remote Sens.* **2024**, *16*, 470. [[CrossRef](#)]
37. Fischer, P.; Wunderlich, T.; Rabbel, W.; Vött, A.; Willershäuser, T.; Baika, K.; Rigakou, D.; Metallinou, G. Combined Electrical Resistivity Tomography (ERT), Direct-Push Electrical Conductivity (DP-EC) Logging and Coring—A New Methodological Approach in Geoarchaeological Research. *Archaeol. Prospect.* **2016**, *23*, 213–228. [[CrossRef](#)]
38. Obrocki, L.; Vött, A.; Wilken, D.; Fischer, P.; Willershäuser, T.; Koster, B.; Lang, F.; Papanikolaou, I.; Rabbel, W.; Reicherter, K. Tracing tsunami signatures of the AD 551 and AD 1303 tsunamis at the Gulf of Kyparissia (Peloponnese, Greece) using direct push in situ sensing techniques combined with geophysical studies. *Sedimentology* **2020**, *67*, 1274–1308. [[CrossRef](#)]
39. Ad-Hoc-Arbeitsgruppe Boden. *Bodenkundliche Kartieranleitung (KA5)*, 5th ed.; Schweizerbart Science Publishers: Stuttgart, Germany, 2005.
40. Köhn, M. Korngrößenanalyse mittels Pipettanalyse. *Tonind.-Ztg.* **1929**, *55*, 729–731.
41. Blume, H.-P.; Stahr, K.; Leinweber, P. *Bodenkundliches Praktikum: Eine Einführung in Pedologisches Arbeiten für Ökologen, Insbesondere Land- und Forstwirte, und für Geowissenschaftler*, 3rd ed.; Springer: Heidelberg, Germany, 2011.
42. Stuiver, M.; Reimer, P.J. Extended C14 data base and revised Calib 3.0 C14 age calibration. *Radiocarbon* **1993**, *35*, 215–230. [[CrossRef](#)]
43. Reimer, P.J.; Austin, W.E.N.; Bard, E.; Bayliss, A.; Blackwell, P.G.; Bronk Ramsey, C.; Butzin, M.; Cheng, H.; Edwards, R.L.; Friedrich, M.; et al. The IntCal20 Northern Hemisphere Radiocarbon Age Calibration Curve (0–55 cal kBP). *Radiocarbon* **2020**, *62*, 725–757. [[CrossRef](#)]
44. Mazzini, I.; Goiran, J.P.; Carbonel, P. Ostracodological studies in archaeological settings: A review. *J. Archaeol. Sci.* **2015**, *54*, 325–328. [[CrossRef](#)]
45. Mazzini, I.; Aiello, G.; Frenzel, P.; Pint, A. Marine and marginal marine Ostracoda as proxies in geoarchaeology. *Mar. Micropaleontol.* **2022**, *174*, 102054. [[CrossRef](#)]
46. Frenzel, P. Fossils of the southern Baltic Sea as palaeoenvironmental indicators in multi-proxy studies. *Quat. Int.* **2019**, *511*, 6–21. [[CrossRef](#)]
47. Athersuch, J.; Horne, D.J.; Whittaker, J.E. *Marine and Brackish Water Ostracods, Synopses of the British Fauna (New Series)*; Brill: Leiden, The Netherlands; New York, NY, USA; Copenhagen, Denmark; Köln, Germany, 1989.
48. Meisch, C. *Süßwasserfauna von Mitteleuropa*; Springer: Berlin/Heidelberg, Germany, 2000.
49. Fuhrmann, R. Atlas quartärer und rezenter Ostrakoden Mitteldeutschlands. In *Altenburger Naturwissenschaftliche Forschungen, vol. 15*; Naturkundemuseum Mauritianum: Altenburg, Germany, 2012.
50. Karanovic, I. Introduction. In *Recent Freshwater Ostracods of the World*; Springer: Berlin/Heidelberg, Germany, 2012; pp. 3–76. [[CrossRef](#)]
51. Birk, J.; Dippold, M.; Wiesenberg, G.L.B.; Glaser, B. Combined quantification of faecal sterols, stanols, stanones and bile acids in soils and terrestrial sediments by gas chromatography–mass spectrometry. *J. Chromatogr. A* **2012**, *1242*, 1–10. [[CrossRef](#)]
52. Leeming, R.; Ball, A.; Ashbolt, N.; Nichols, P. Using faecal sterols from humans and animals to distinguish faecal pollution in receiving waters. *Water Res.* **1996**, *30*, 2893–2900. [[CrossRef](#)]
53. Frenzel, P.; Schulze, I.; Pint, A. Noding of *Cyprideis torosa* valves (Ostracoda)—A proxy for salinity? New data from field observations and a long-term microcosm experiment. *Int. Rev. Hydrobiol.* **2012**, *97*, 314–329. [[CrossRef](#)]
54. Pint, A. Ostrakoden und Foraminiferen aus Athalassischen Gewässern und Deren Anwendung für die Rekonstruktion Quartärer Ökosysteme. Ph.D. thesis, Friedrich-Schiller-Universität Jena, Jena, Germany, 2016; p. 207.

55. Pint, A.; Frenzel, P. Ostracod fauna associated with *Cyprideis torosa*—An overview. *J. Micropalaeontol.* **2017**, *36*, 113–119. [[CrossRef](#)]
56. Matzanas, C. Die Kladeos-Ufermauer. In *Mythos Olympia. Kult und Spiele*; Heilmeyer, W.-D., Kaltsas, N., Gehrke, H.-J., Hatzi, G.E., Bocher, S., Eds.; Prestel: München, Germany, 2012; pp. 238–239.
57. Khan, M.N.; Mohammad, F. Eutrophication: Challenges and solutions. In *Eutrophication: Causes, Consequences and Control*; Abid Ansari, A., Gill, S.S., Lanza, G.R., Rast, W., Eds.; Springer: Dordrecht, The Netherlands, 2014; pp. 1–15.
58. Bhagowati, B.; Ahamad, K.U. A review on lake eutrophication dynamics and recent developments in lake modeling. *Ecolhydrol. Hydrobiol.* **2019**, *19*, 155–166. [[CrossRef](#)]
59. Ruiz, F.; Abad, M.; Bodergat, A.M.; Carbonel, P.; Rodríguez-Lázaro, J.; González-Regalado, M.L.; Toscano, A.; García, E.X.; Prenda, J. Freshwater ostracods as environmental tracers International. *J. Environ. Sci. Technol.* **2013**, *10*, 1115–1128. [[CrossRef](#)]
60. Aydin, K. Baden wie die Römer—Badespaß, Saunaguss und Wellness pur. In *Wasserwelten. Badekultur und Technik. Begleitschrift Zur Ausstellung Wasserwelten im Landesmuseum Natur und Mensch Oldenburg 15. August–17. Oktober 2010*; Philipp von Zabern: Darmstadt, Germany, 2010; pp. 89–101.
61. Brödner, E. *Römische Thermen und Antikes Badewesen*; Wissenschaftliche Buchgesellschaft: Darmstadt, Germany, 2011.
62. Künzl, E. *Die Thermen der Römer*; Wissenschaftliche Buchgesellschaft: Darmstadt, Germany, 2013.
63. Trümper, M. Greek Swimming Pools—Case Study of Olympia Cura aquarum in Greece. *Schriften Dtsch. Wasserhistorischen Ges.* **2017**, *27*, 215–250.
64. Baeten, J.; Marinova, E.; De Laet, V.; Degryse, P.; De Vos, D.; Waelkens, M. Faecal biomarker and archaeobotanical analyses of sediments from a public latrine shed new light on ruralisation in Sagalassos, Turkey. *J. Archaeol. Sci.* **2012**, *39*, 1143–1159. [[CrossRef](#)]
65. Marriner, N.; Morhange, C. Geoscience of ancient Mediterranean harbours. *Earth-Sci. Rev.* **2007**, *80*, 137–194. [[CrossRef](#)]
66. Finkler, C. The Geological Record of Ancient Harbours: Using Ancient Harbour Gearchives of Corcyra (Greece) to Reconstruct the Palaeoenvironmental Development and to Identify Extreme Events by Means of a Multi-Proxy Based Geoarchaeological Approach. Ph.D. Thesis, Johannes Gutenberg-Universität Mainz, Mainz, Germany, 2018. [[CrossRef](#)]
67. Hadler, H.; Vött, A.; Koster, B.; Mathes-Schmidt, M.; Mattern, T.; Ntageretzis, K.; Reicherter, K.; Willershäuser, T. Multiple late-Holocene tsunami landfall in the eastern Gulf of Corinth recorded in the palaeotsunami geo-archive at Lechaion, harbour of ancient Corinth (Peloponnese, Greece). *Z. Geomorphol. Suppl. Issues* **2013**, *57*, 139–180. [[CrossRef](#)]
68. Hadler, H.; Baika, K.; Pakkanen, J.; Evangelistis, D.; Emde, K.; Fischer, P.; Ntageretzis, K.; Röbbke, B.R.; Willershäuser, T.; Vött, A. Palaeotsunami impact on the ancient harbour site Kyllini (western Peloponnese, Greece) based on a geomorphological multi-proxy approach. *Z. Geomorphol. Suppl. Issues* **2015**, *59*, 7–41. [[CrossRef](#)]
69. Finkler, C.; Fischer, P.; Baika, K.; Rigakou, D.; Metallinou, G.; Hadler, H.; Vött, A. Tracing the Alkinoos Harbor of ancient Kerkyra, Greece, and reconstructing its paleotsunami history. *Geoarchaeology* **2018**, *33*, 24–42. [[CrossRef](#)]
70. Ashton, N.; Lewis, S.G.; Stringer, C. (Eds.) The Ancient Human Occupation of Britain. In *Developments in Quaternary Sciences, Vol. 14*; AHOB Publications: Amsterdam, The Netherlands, 2011.
71. Ambraseys, N. *Earthquakes in the Mediterranean and Middle East. A Multidisciplinary Study of Seismicity up to 1900*; Cambridge University Press: Cambridge, UK, 2009.
72. Hadler, H.; Willershäuser, T.; Ntageretzis, K.; Henning, P.; Vött, A. Catalogue entries and non-entries of earthquake and tsunami events in the Ionian Sea and the Gulf of Corinth (eastern Mediterranean, Greece) and their interpretation with regard to palaeotsunami research. In *Beiträge der 29. Jahrestagung des Arbeitskreises “Geographie der Meere und Küsten”, 28. bis 30. April 2011 in Bremen*; Vött, A., Venzke, J.-F., Eds.; Bremer Beiträge zur Geographie und Raumplanung, Vol. 44; Institut für Geographie: Erlangen, Germany, 2012; pp. 1–167. Available online: <https://www.geomorphologie.uni-mainz.de/files/2013/10/AMK29.pdf> (accessed on 27 November 2024).
73. Karkani, A.; Evelpidou, N.; Tzouxanioti, M.; Petropoulos, A.; Gogou, M.; Mloukie, E. Tsunamis in the Greek region: An Overview of Geological and Geomorphological Evidence. *Geosciences* **2022**, *12*, 4. [[CrossRef](#)]
74. Stiros, S. The AD 365 Crete earthquake and possible seismic clustering during the fourth to sixth centuries AD in the Eastern Mediterranean: A review of historical and archaeological data. *J. Struct. Geol.* **2001**, *23*, 545–562. [[CrossRef](#)]
75. Cleland, P.H.F. The Crime of Archeology—A Study of Weathering. *Sci. Mon.* **1932**, *35*, 169–173.

**Disclaimer/Publisher’s Note:** The statements, opinions and data contained in all publications are solely those of the individual author(s) and contributor(s) and not of MDPI and/or the editor(s). MDPI and/or the editor(s) disclaim responsibility for any injury to people or property resulting from any ideas, methods, instructions or products referred to in the content.